

DISCOVERY OF BROAD MOLECULAR LINES AND OF SHOCKED MOLECULAR HYDROGEN FROM THE SUPERNOVA REMNANT G357.7+0.3: HHSMT, APEX, *SPITZER* AND SOFIA OBSERVATIONSJ. RHO<sup>1,2</sup>, J. W. HEWITT<sup>3,4</sup>, J. BIEGING<sup>5</sup>, W. T. REACH<sup>6</sup>, M. ANDERSEN<sup>7</sup>, AND R. GÜSTEN<sup>8</sup>

Draft version February 21, 2022

## ABSTRACT

We report a discovery of shocked gas from the supernova remnant (SNR) G357.7+0.3. Our millimeter and submillimeter observations reveal broad molecular lines of CO(2-1), CO(3-2), CO(4-3), <sup>13</sup>CO (2-1) and <sup>13</sup>CO (3-2), HCO<sup>+</sup> and HCN using HHSMT, Arizona 12-Meter Telescope, APEX and MOPRA Telescope. The widths of the broad lines are 15-30 km s<sup>-1</sup>, and the detection of such broad lines is unambiguous, dynamic evidence showing that the SNR G357.7+0.3 is interacting with molecular clouds. The broad lines appear in extended regions (>4.5'×5'). We also present detection of shocked H<sub>2</sub> emission in mid-infrared but lacking ionic lines using the *Spitzer* IRS observations to map a few arcmin area. The H<sub>2</sub> excitation diagram shows a best-fit with a two-temperature LTE model with the temperatures of ~200 and 660 K. We observed [C II] at 158μm and high-J CO(11-10) with the GREAT on SOFIA. The GREAT spectrum of [C II], a 3σ detection, shows a broad line profile with a width of 15.7 km s<sup>-1</sup> that is similar to those of broad CO molecular lines. The line width of [C II] implies that ionic lines can come from a low-velocity C-shock. Comparison of H<sub>2</sub> emission with shock models shows that a combination of two C-shock models is favored over a combination of C- and J-shocks or a single shock. We estimate the CO density, column density, and temperature using a RADEX model. The best-fit model with n(H<sub>2</sub>) = 1.7×10<sup>4</sup> cm<sup>-3</sup>, N(CO) = 5.6×10<sup>16</sup> cm<sup>-2</sup>, and T = 75 K can reproduce the observed millimeter CO brightnesses.

*Subject headings:* radio lines: ISM - infrared: ISM - ISM:supernova remnants - ISM:individual objects (G357.7+0.3)

## 1. INTRODUCTION

Supernovae (SNe) are among the most violent events in the Universe, ejecting gas and returning material from dense molecular clouds into the more diffuse interstellar medium and the galactic halo. When the expanding blast wave encounters a dense molecular cloud, the SN shocks drive excitation, chemical reaction, and dynamic motion of the gas, and destroy dust grains by collisions or thermal sputtering (Jones et al. 1994; Andersen et al. 2011). This interaction may determine the fate of the molecular cloud, either dispersing it or triggering collapse of dense cores leading to a subsequent generation of star formation.

A few signs of molecular clouds and SN (MC-SN or MC-SNR) interactions have been found such as *Mixed-morphology* SNRs, or detections of OH masers and molecular hydrogen (H<sub>2</sub>). A signpost of the in-

teraction is center-filled, thermal X-ray emission (e.g. Rho & Petre 1998; Pannuti et al. 2014, and references therein) that can be produced through thermal conduction (Tilley et al. 2006a,b; Orlando et al. 2009). However, it is still not clear if the interaction with clouds is a unique mechanism to produce Mixed-morphology SNRs. A better indicator of SN-MC interactions is the presence of 1720 MHz OH masers which are detected from ~20 SNRs (Frail et al. 1996; Yusef-Zadeh et al. 1999; Hewitt et al. 2008). These masers are thought to be collisionally excited and they suggest SN-MC interactions, but maser emission is not well understood (Yusef-Zadeh et al. 1999). In 3C391, a maser position in the southwestern shell is correlated with broad CO lines, but a maser position in the northeastern shell show only narrow CO lines (Reach & Rho 1999). Other evidence of shock interaction with clouds is H<sub>2</sub> emission from collisionally excited shocked gas, but the H<sub>2</sub> emission could also originate from UV pumping (Burton et al. 1992). Examples of collisionally excited H<sub>2</sub> emission from shock interaction with molecular clouds are IC 443 (Burton et al. 1990; Richter, Graham & Write 1995), W44 and W28 (Reach, Rho & Jarrett 2005; Neufeld et al. 2007). A one-to-one correspondence between H<sub>2</sub> and broad CO emission has been found in IC 443 (Rho et al. 2001). Eighteen interacting remnants are found using infrared (IR) colors from the *Spitzer* GLIMPSE data (Reach et al. 2006). Follow-up *Spitzer* spectroscopy confirms detection of H<sub>2</sub> lines as well as ionic fine-structure lines and shock-processed dust (Hewitt et al. 2009; Andersen et al. 2010).

A strong correlation between molecular interacting SNRs and γ-ray emission has been known since the

<sup>1</sup> SETI Institute, 189 N. Bernardo Ave., Mountain View, CA 94043; jrho@seti.org

<sup>2</sup> SOFIA Science Center, NASA Ames Research Center, MS211-1, Moffett Field, CA 94043

<sup>3</sup> CRESST/University of Maryland, Baltimore County, Baltimore, MD 21250 and NASA Goddard Space Flight Center, Greenbelt, MD 20771, USA

<sup>4</sup> University of North Florida, Dept. of Physics, Jacksonville, FL 32224; john.w.hewitt@unf.edu

<sup>5</sup> Steward Observatory, The University of Arizona, Tucson AZ 85721, USA; jbieging@as.arizona.edu

<sup>6</sup> Universities Space Research Association, SOFIA Science Center, NASA Ames Research Center, MS 232, Moffett Field, CA 94034; wreach@sofia.usra.edu

<sup>7</sup> Gemini Observatory, Casilla 603, La Serena, Chile, manderse@gemini.edu

<sup>8</sup> Max Planck Institut für Radioastronomie, Auf dem Hügel 69, 53121 Bonn, Germany, gusten@mpifr-bonn.mpg.de

EGRET era (Esposito et al. 1996). Recently Fermi and HESS observations revealed extended  $\gamma$ -ray emission associated with molecular interacting SNRs like IC 443 (Abdo et al. 2010a), W44 (Uchiyama et al. 2010; Abdo et al. 2010c) and W28 (Hanabata et al. 2014; Aharonian et al. 2008; Abdo et al. 2010b), emphasizing the astrochemical processes of molecules and hadronic particles by SNe. The  $\gamma$ -ray emission is associated with shocked molecular material previously identified with millimeter (mm) CO and infrared H<sub>2</sub> emission (Burton et al. 1990; Reach & Rho 2006; Reach, Rho, & Jarrett 2005). With *Fermi* observations, there is a growing number of  $\gamma$ -ray emitting SNRs, many of which have the indicators of MC-SNR interactions described above (Abdo et al. 2009; Hewitt et al. 2012; Wu et al. 2011; Daniel & Slane 2010; Hewitt et al. 2015, and references therein). The study of MC-SNR interactions is advancing rapidly because of multi-wavelength observations; strong correlations among them provide opportunities to discover true samples of SNRs interacting with clouds.

The clearest evidence for interaction between SNRs and molecular clouds is the detection of emission from the shocked molecules themselves. Millimeter observations provide direct, unambiguous evidence of interaction when a broad ( $>10$  km s<sup>-1</sup>) line caused by dynamic motion of shocked gas is detected. There has been a long-term effort to search for interactions with clouds using millimeter observations (Huang & Thaddeus 1986; Jeong et al. 2013; Zhou et al. 2014; Liszt 2009). However, detection of broad CO lines is still limited to a half dozen SNRs. Millimeter observations of SNRs which have evidence of shocks by showing broad lines are IC 443 (e.g. van Dishoeck et al. 1993, references therein), W44 (Wootten 1997; Reach, Rho & Jarrett 2005; Seta et al. 2004; Anderl, Gusdorf, & Güsten 2014), W28 (Arikawa et al. 1999; Reach, Rho & Jarrett 2005), 3C391 (Reach & Rho 1999), W51C (Koo & Moon 1997), and HB21 (Koo et al 2001; Shinn et al. 2010). For some cases, changes in CO velocity profiles or a small amount of broadening in the line profiles may indicate interactions with clouds (Dubner et al. 2004; Zhou et al. 2011). Recently Kilpatrick et al. (2016, 2014) observed SNRs emitting  $\gamma$ -ray emission using HESS and detected evidence of interaction in millimeter from a few SNRs. Another example of broad molecular lines is a water line at 557 GHz from the SNR G349.7+0.2 (with a FWHM of 144 km s<sup>-1</sup>) using Herschel HIFI observations (Rho et al. 2015). IC 443 is another case showing a broad infrared water line (Snell et al 2005).

The SNR G357.7+0.3 is relatively unknown and understudied. Radio observations identified this source as a SNR (Reich & Fürst 1984). It is named “Square Nebula” because of its square-like radio morphology as shown in Figure 1. Soft, faint blobs of X-ray emission using *Einstein IPC* have been detected with an inferred temperature of  $5.4 \times 10^6$  K and an age of 10,000 yr (Leahy 1989). OH masers have been detected around -35 km s<sup>-1</sup> (Yusef-Zadeh et al. 1999) and they are shown to be extended from the western edge (Hewitt et al. 2008). A study of surrounding material of the SNR using *Spitzer* IRAC images by Phillips et al. (2009); Phillips & Marquez-Lugo (2010) provides circumstantial

evidence of interacting with molecular clouds, but its direct evidence still lacks. There is no previous detection of this SNR in optical or infrared. The distance to G357.7+0.3 is 6.4 kpc which is consistent with -35 km s<sup>-1</sup> (from OH lines) in Galactic rotation curve (see Yusef-Zadeh et al. 1999).

In this paper, we report direct evidence that the SNR G357.7+0.3 interacts with molecular clouds resulting in broad millimeter lines (such as CO and HCO<sup>+</sup>). The dynamic motion is revealed in the shocked clouds. We also report detection of shocked H<sub>2</sub> emission in mid-infrared from G357.7+0.3 using *Spitzer* spectroscopy IRS data. Section 2 describes observations which include 10 independent observing runs (see Table 1). In Section 3.1, we report direct evidence that the SNR G357.7+0.3 interacts with molecular clouds with broad millimeter lines (such as CO and HCO<sup>+</sup>) using ground-based telescopes. Spectral mapping of CO lines is described in Section 3.2 and 3.3. The detection of an atomic line of [C II] at 158  $\mu$ m and the upper limit of high-J CO line in Section 3.4. Large-scale molecular cloud maps surrounding the SNR are presented in Section 3.5. The detection of molecular hydrogen line with *Spitzer* IRS is in Section 3.6. In Section 4, we discuss the physical conditions of shocked gas including excitation of molecular hydrogen and CO gas. Our paper presents the first direct evidence that the SNR G357.7+0.3 interacts with molecular clouds. Because SNR-MC interactions are valuable astrophysical laboratories, our paper provides a new and exciting laboratory where molecular astro-chemistry and shocks can be studied.

## 2. OBSERVATIONS

We performed ten independent observing runs using ground-based telescopes, *Spitzer* Space telescope, and the Stratospheric Observatory for Infrared Astronomy (SOFIA) air-borne telescope over a time span of more than 10 years. The ground-based observing runs are using Heinrich Hertz Submillimeter Telescope (HHSMT), 12-Meter (12-m, hereafter) Kitt Peak telescope, and Atacama Pathfinder Experiment (APEX) telescope. The observational dates are summarized in Table 1. The positions of G357.7+0.3 we observed are listed in Table 2 and marked on Figure 1. All maps in this paper have equatorial coordinates in J2000.

### 2.1. HHSMT observations

We performed mm and submillimeter (submm) observations of G357.7+0.3 using the HHSMT (or SMT)<sup>1</sup> located at Mt. Graham, Arizona centered on one of the OH maser positions, OH-A1 of G357.7+0.3 (R.A. 17<sup>h</sup>38<sup>m</sup>30.39<sup>s</sup> and Dec. -30° 33'17", J2000) on 2003 May 18-19 and June 8 and 2006 March 3-4. We observed <sup>12</sup>CO(3-2) and <sup>12</sup>CO(2-1) using acousto-optic spectrometer (AOS) and filterbank. The AOS spectra (see Figure 2) were measured with a 2048-channel, 1 GHz total bandwidth AOS with an effective resolution of 1 MHz. The observations were made with three facility SIS mixer receivers placed at the Nasmyth focus. The beam efficiencies of single-polarization receivers in the frequency bands 210 - 275 GHz and 430 - 480 GHz are 0.77 (an

<sup>1</sup> <http://www.as.arizona.edu/aro/>

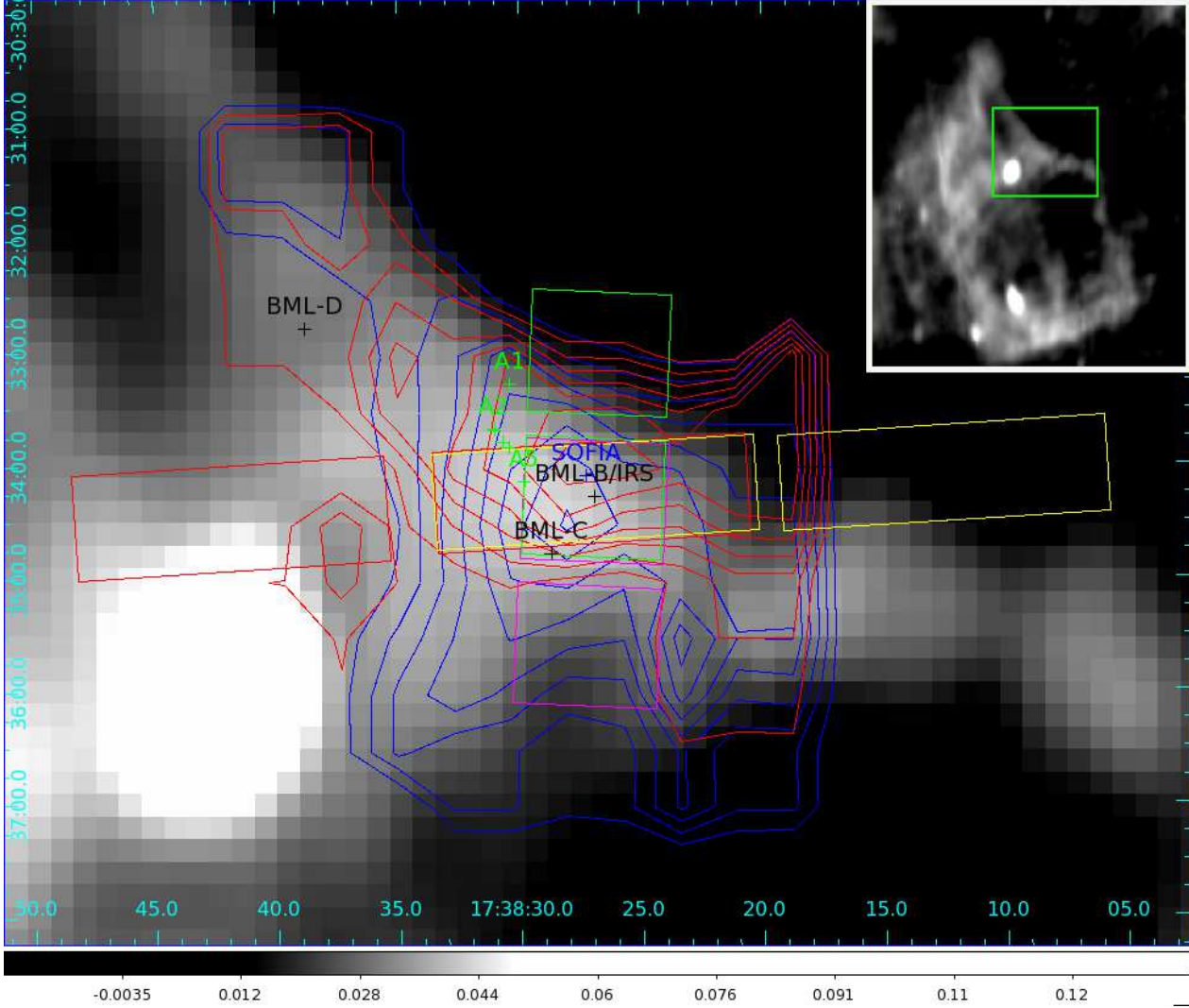


FIG. 1.— The positions of OH masers from Yusef-Zadeh et al. (1999, crosses in green), CO broad molecular lines (BML; crosses in black), and the center (the same as BML-B) and fields of view (marked in rectangular boxes) of *Spitzer* IRS (in green for SL1, magenta for SL2, red for LL2, and yellow for LL1) are marked on the northwestern part of radio image of G357.7+0.3. The field of view is shown in the radio image of the entire SNR (in the inserted image marked as a box in green). The contours are from CO broad molecular line maps (blue-wing in blue and red-wing in red; see Section 3.2 for details). The 20 cm radio continuum image shows  $32' \times 35'$  field of view (FOV) centered on R.A.  $17^{\text{h}}38^{\text{m}}36.5^{\text{s}}$  and Decl.  $-30^{\circ}37'26.2''$  (J2000), and the scale of color bar has a unit of Jy/beam (synthesized beam of  $15''$ ).

TABLE 1  
SUMMARY OF MILLIMETER AND INFRARED OBSERVATIONS

Date	Telescope	Lines
2003 May 18, 19	HHSMT	CO(2-1)
2003 Jun 8	HHSMT	CO(2-1)
2005 August 14	Spitzer IRS	H <sub>2</sub>
2006 March 3, 4	HHSMT	CO(3-2)
2006 March 6-9	ARO 12-Meter	<sup>13</sup> CO(1-0), HCO <sup>+</sup>
2006 April 14, 15	ARO 12-Meter	<sup>13</sup> CO(1-0) maps
2007 September 19	MOPRA	HCO <sup>+</sup> (1-0), HCN(1-0) etc
2013 July 18	SOFIA GREAT	[C II], CO(11-10)
2015 April 16	APEX (Obs. 1) SHeFI	CO(2-1), <sup>13</sup> CO(2-1)
2015 August 16, 17	APEX (Obs. 2) FLASH, SHeFI	CO(4-3), CO(3-2), <sup>13</sup> CO(3-2)



TABLE 2  
OBSERVED POSITIONS OF G357.7+0.3

Position	Offset	R.A., Decl.
OH-A1/BML-A	(0,0)	17:38:30.39,-30:33:17.7
APEX Obs. 2	(0,0)	17:38:30.39,-30:33:17.7
OH-A2	(+9.8,-23)	17:38:30.39,-30:33:17.7
BML-B	(-60,-60)	17:38:26.9,-30:34:17.7
<i>Spitzer</i> IRS	(-60,-60)	17:38:26.9,-30:34:17.7
MOPRA	(-50,-50)	17:38:27,-30:34:08
SOFIA (H <sub>2</sub> peak)	(-48,-48)	17:38:27.25,-30:34:06.4
APEX Obs. 1	(-60,-60)	17:38:26.9,-30:34:08
BML-C	(-30,-90)	17:38:28.7,-30:34:47.7
BML-D	(+60,+30)	17:38:38.8,-30:32:47.7

example of CO(2-1)) and 0.45, and a dual-polarization receivers covering the frequency band 320 - 375 GHz is 0.48 for CO (3-2). The telescope beam size is  $34''$  at 217 GHz,  $22''$  at 347 GHz, and  $18''$  at 434 GHz. One of challenges of observation is to find a clear reference position since the SNR is located at the Galactic plane; we tried 2-10 positions and verified the emission from the reference positions were clear. The final reference position used is RA.  $17^{\text{h}}35^{\text{m}}15.5^{\text{s}}$  and Dec.  $-30^{\circ}10'48''$  (J2000).

We performed spectral GRID mapping ( $10 \times 10$  spectra) in CO(2-1) covering  $4.5' \times 5'$  area with a spacing of  $30''$  centered on BML-B position using HHSMT. Details are described in Section 3.2.

### 2.2. 12-Meter Telescope observations

The 12-Meter Telescope is located on Kitt Peak and is one of the Arizona Radio Observatory Telescopes. We observed the SNR G357.7+0.3 on 2006, March 6-16 and the lines we observed are  $^{13}\text{CO}$  (1-0) and  $\text{HCO}^+$  (1-0) (see Table 3). We observed a few positions for  $\text{HCO}^+$  lines and a large  $^{13}\text{CO}$ (1-0) map of  $30' \times 35'$  area covering the SNR G357.7+0.3 and its surroundings.

### 2.3. *Spitzer* IRS observations

We performed an IRS spectral mapping centered on the northwestern shell of G357.7+0.3 (R.A.  $17^{\text{h}}38^{\text{m}}26.9^{\text{s}}$  and Dec.  $-30^{\circ}34'17.7''$ , J2000; position “BML-B” which is a peak of CO broad molecular line (BML) as a part of *Spitzer* IRAC GTO time (PI: Giovanni Fazio).

The short-low (SL:  $8\text{--}15\ \mu\text{m}$ ) covered  $75'' \times 60''$  (supplement data covered the same area in the south for SL2, and in the north for SL1), and long-low (LL) covered  $170'' \times 55''$  (supplementary data covered the same area to the west for SL2, and to the east for LL1). The Long Low (LL:  $15\text{--}40\ \mu\text{m}$ ) IRS data were taken on 2005 August 14 with 6 cycles of 30 sec exposure time; this yields a total exposure time of 360 sec for the first and second staring positions. The SL IRS observations were made with 3 cycles of 60 sec exposure time and one cycle covers 2 dither positions; this yields a total exposure time of 360 sec per sky position. The spatial resolution ( $=1.2 \times \lambda/D$  sr where D is 85 cm for *Spitzer*) of H<sub>2</sub> image generated from the IRS data is approximately  $2'', 3'', 3.6'', 5''$  and  $8.3''$  at 6.9, 9.6, 12.2, 17, and  $28\ \mu\text{m}$ , respectively. The IRS spectra (AORkey of 21819136) were processed using the S18.8 pipeline products and reduced using CUBISM. The spectra are extracted for the bright part of

H<sub>2</sub> emission with a rectangular region of  $40'' \times 50''$  centered on the IRS position of R.A.  $17^{\text{h}}38^{\text{m}}26.9^{\text{s}}$  and Dec.  $-30^{\circ}34'17.7''$  (J2000) as shown in Figure 1. The region is the overlapped region among SL1, SL2, LL2 and LL1.

### 2.4. MOPRA observations

Observations of selected positions were obtained using the 22m Australia Telescope MOPRA<sup>2</sup> antenna during September 2007. G357.7+0.3 was observed using the MOPS spectrometer backend configured in zoom mode to simultaneously observe 16 windows within an 8.3 GHz bandwidth in both linear polarizations. Each window has 137.5 MHz sampled over 4096 channels. Final spectra (see Figure 10) are smoothed with a four-channel Gaussian function, giving a velocity resolution of  $0.44\ \text{km s}^{-1}$  at 90 GHz. For all sources we observed  $\text{C}^{34}\text{S}$  (2-1) at 96.4 GHz,  $\text{CH}_3\text{OH}$  (2-1) at 95.9 GHz,  $\text{CH}_3\text{OH}$  (8-7) at 95.1 GHz,  $\text{N}_2\text{H}^+$  (1-0) at 93.2 GHz,  $^{13}\text{CS}$  (2-1) at 92.5 GHz,  $\text{HNC}$  (1-0) at 90.7 GHz,  $\text{HCO}^+$  (1-0) at 89.2 GHz, and  $\text{HCN}$  (1-0) at 88.7 GHz.  $\text{HCN}$  J=1-0 is a triplet with F=2-1, 1-1, 0-1 at 88.631847, 88.630416 and 88.633936 GHz, respectively. When fitting this line we fit the F=2-1 line and assume the two other lines of the triplet are found at a fixed velocity separation of  $+4.84, -7.08\ \text{km s}^{-1}$  and fixed line strengths relative to F=2-1 of 0.5, 0.25 for the F=1-1, F=1-0 transitions respectively. The main beam efficiency,  $T_{mb}$ , is 0.4-0.49 in the band (Ladd et al. 2005).

$\text{HCO}^+$  and  $\text{HCN}$  lines are detected as shown in Figure 10 (see Section 3.2 for details), and the upper limit of  $\text{C}^{34}\text{S}$ (2-1),  $\text{CH}_3\text{OH}$  (2-1),  $\text{CH}_3\text{OH}$  (8-7),  $\text{N}_2\text{H}^+$ (1-0),  $^{13}\text{CS}$  (2-1), and  $\text{HNC}$  (1-0) is 0.05 K for each.

### 2.5. APEX observations

APEX observations were conducted on 2015 April 16 and on 2015 August 16 and 17. The observing time of 2015 April 16 observations was granted (PI: Andersen) from ESO open proposal call, and 2015 August time is through APEX instrument PI allocated time. We used SHFi, FLASH345, and FLASH460 (Heyminck et al. 2006). The beam efficiency of CO(3-2) and CO (4-3) are 0.73, and 0.60, respectively, and the beam sizes are listed in Table 3. The data were reduced in CLASS<sup>3</sup> and the final results were exported into IDL.

### 2.6. SOFIA Observations

We observed the SNR G357.7+0.3 with the German Receiver for Astronomy at Terahertz Frequencies (GREAT) (Heyminck et al. 2012) on board the SOFIA airborne observatory (Young et al. 2012). GREAT is a far-infrared high resolution spectrometer with a resolving power of  $\sim 10^6$ . Only low frequency detectors covering 1.25 - 1.5 THz (wavelengths of 240 -  $200\ \mu\text{m}$ ; L1) and 1.82 - 1.92 THz ( $165 - 156\ \mu\text{m}$ ; L2) were available during the cycle 1. The observation was a program (proposal ID of O1\_0059; PI: Hewitt) of Guest Observer cycle 1 campaign. Five hrs of observation time was awarded, but a total of  $\sim 2$  hrs ( $\sim 1$  hr on July 18 and  $\sim 1$  hr on July 28) were included in the flight series and the flights for remaining observing time of 3 hrs were cancelled. The

<sup>2</sup> <http://www.narrabri.atnf.csiro.au/mopra/obsinfo.html>

<sup>3</sup> See <http://www.iram.fr/IRAMFR/GILDAS>

TABLE 3  
SUMMARY OF MOLECULAR LINE PROPERTIES

Position	line	Frequency (GHz)	Telescope [beam size (")]	$V_{lsr}$ (km s <sup>-1</sup> )	FWHM (km s <sup>-1</sup> )	$\int T dv$ (K km s <sup>-1</sup> )	RMS (K)	$t_{int}$ (min)
OH-A1	CO (2-1)	230.5379	HHSMT [30]	-35.46±0.17	17.23±0.58	89.94±1.83	0.125	22
OH-A1	CO (2-1)	230.5379	APEX SHeFI [30]	-35.85±0.16	18.37±0.53	90.08±1.99	0.106	11
OH-A1	CO (3-2)	345.7959	HHSMT [22]	-35.86±0.07	17.33±0.20	163.64±1.35	0.189	18
OH-A1	CO (3-2)	345.7959	APEX FLASH [22]	-35.18±0.06	17.26±0.18	90.09±0.64	0.068	21
OH-A1	CO (4-3)	461.0407	APEX FLASH [13]	-34.65±0.04	14.71±0.10	64.29±0.33	0.134	43
OH-A1	<sup>13</sup> CO(1-0)	110.2013	ARO 12-m [47]	-35.07±0.10	3.95±0.31	4.57±0.26	0.100	20
OH-A1	<sup>13</sup> CO(2-1)	220.3986	APEX SHeFI (30)	-34.89±0.07	7.52±0.23	7.09±0.16	0.056	27
OH-A1	<sup>13</sup> CO(3-2)	330.5879	APEX FLASH [22]	-34.73±0.14	10.76±0.39	4.22±0.12	0.040	21
OH-A1	HCO <sup>+</sup>	89.1885	ARO 12-m [58]	-33.47±0.34	25.03±0.94	4.04±0.12	0.017	123
BML-B	CO (2-1)	230.5379	APEX-1 (SHeFI) [28]	-34.04±0.09	26.79±0.19	111.52±0.71	0.077	6
BML-B	CO (3-2)	345.7959	HHSMT [22]	-35.21±0.08	22.01±0.19	200.50±1.42	0.145	14
BML-B	<sup>13</sup> CO(2-1)	220.3986	APEX (SHeFI) [28]	-34.932±0.231	16.67±0.60	6.28±0.18	0.073	6
BML-B	HCO <sup>+</sup> (1-0)	89.1885	ARO 12-m [58]	-33.56±0.01	27.96±0.02	4.88±1.30	0.012	98
BML-B	HCO <sup>+</sup> (1-0)	89.1885	MOPRA [38]	-34.75±0.01	25.16±0.01	3.16±0.82	0.023	68
BML-B	HCN (1-0)	88.6316	MOPRA [38]	-32.16±0.01	27.25±0.01	2.67±0.74	0.024	68
BML-B	[C II]	1900.5369	SOFIA GREAT [14.1]	-30.32±1.54	15.69±3.34	5.61±1.08	0.110	4.9

observation of G357.7+0.3 took place on 2013 July 18 toward the peak of H<sub>2</sub> emission as listed in Table 3. The observed integration time for [C II] and CO (11-10) lines are 5 min for each, because the first block of observations toward the first position of G357.7+0.3 was lost due to tracking and wobbler issues. Successful observing time was about 30 min on July 18. Note that the efficiencies of SOFIA flights and observations have been significantly improved since 2014. The observations made a map of 1'×1', but since the signal is very weak, we have averaged the spectrum over the area (see Figures 12 and 13). The main beam efficiencies of 0.67 were used for both of the GREAT channels L1 & L2.

### 3. RESULTS

#### 3.1. Broad millimeter lines from shocked gas

Figure 2 (the second panel) shows the <sup>12</sup>CO (3-2) line toward the OH-A1 position of G357.7+0.3 observed with HHSMT. The spectrum shows a broad line with a FWHM of 17.32 km s<sup>-1</sup> at a velocity of -35.86 km s<sup>-1</sup> (see Table 3) and a narrow (~ 4 km s<sup>-1</sup>) absorption dip at -35.30 km s<sup>-1</sup>. Such a broad line is caused by strong SN shocks passing through dense molecular clouds, and the detection of such broad lines is direct, unambiguous evidence that G357.7+0.3 is a SNR interacting with molecular clouds. Figure 1 shows the area (over 4.5'×5') where broad lines are detected (see Section 3.2 for details). Figure 2 includes other millimeter molecular lines of <sup>13</sup>CO(1-0), <sup>12</sup>CO(2-1), and HCO<sup>+</sup> observed with HHSMT and 12-m telescopes. HCO<sup>+</sup> spectrum has a lower signal-to-noise than those of CO(3-2) and CO(2-1), but the line profile is the same as those of the other two lines, indicating that the HCO<sup>+</sup> line also shows a broad line with a self-absorption. Both of <sup>12</sup>CO(2-1) and HCO<sup>+</sup> spectra show similar profiles to that of <sup>12</sup>CO(3-2) with the widths of ~20-30 km s<sup>-1</sup>. We fit each spectrum either using a gaussian profile with a mask of the velocity range of the self-absorption line, or two gaussian components with a broad emission line and a narrow absorption line. The results from the two methods yielded similar

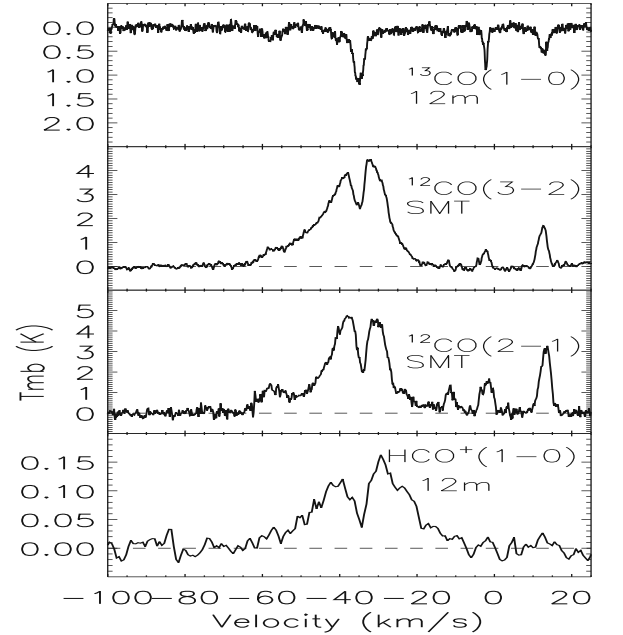


FIG. 2.— CO and HCO<sup>+</sup> spectra of G357.7+0.3 using HHSMT and 12-m telescope. The velocity range is from -100 to 25 km s<sup>-1</sup>. <sup>13</sup>CO(1-0) line is shown from positive to negative, in order to demonstrate the emission causes the absorption dip in the broad lines of <sup>12</sup>CO(3-2), <sup>12</sup>CO(2-1), and HCO<sup>+</sup>.

results and are summarized in Table 3. The RMS noises are obtained using a long baseline typically between -200 and 100 km s<sup>-1</sup>. An example of a spectral fit is shown in Figure 3. The line properties (e.g. for broad lines) are summarized in Table 3.

We observed additional CO lines with APEX, which offers simultaneous observations of three lines. The spectra of <sup>12</sup>CO(2-1), <sup>12</sup>CO(3-2), <sup>12</sup>CO(4-3), <sup>13</sup>CO(2-1) and <sup>13</sup>CO(3-2) are shown in Figure 4. The CO lines of <sup>12</sup>CO(4-3), <sup>13</sup>CO(2-1) and <sup>13</sup>CO(3-2) were only observed with APEX. The <sup>13</sup>CO(3-2) line shows a broad line, and

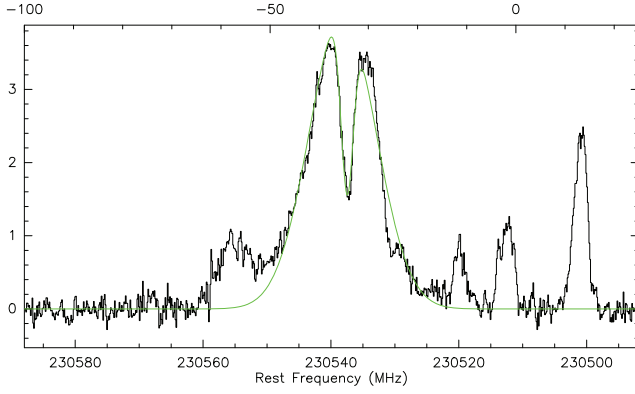


FIG. 3.— HHSMT CO(2-1) spectrum superposed on spectral model fit. The fit is a combination of a broad emission line between  $-55$  and  $-20$   $\text{km s}^{-1}$  and a narrow absorption line between  $-32$  and  $-38$   $\text{km s}^{-1}$ .

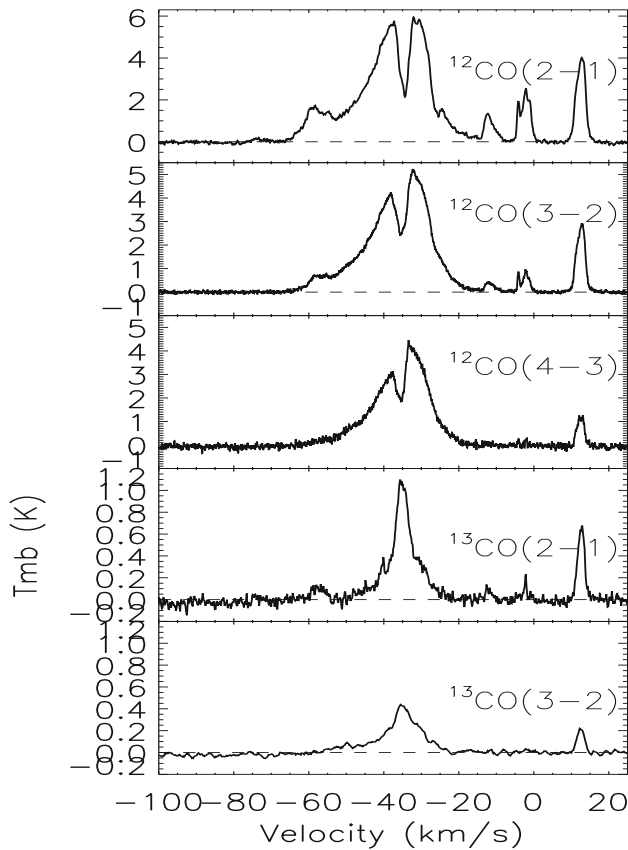


FIG. 4.— APEX spectra of G357.7+0.3 in CO(2-1), CO(3-2), CO(4-3),  $^{13}\text{CO}$  (2-1), and  $^{13}\text{CO}$  (3-2) lines.

$^{13}\text{CO}$ (2-1) show a combination of a broad line similar to the one in  $^{13}\text{CO}$ (3-2) and a narrow emission line similar to the one in  $^{13}\text{CO}$ (1-0).

### 3.2. Spectral mapping of CO(2-1)

Spectral GRID mapping was made in CO(2-1) using the HHSMT for a  $4.5' \times 5'$  area. The GRID spectra are shown in Figure 5, and a typical RMS of CO(2-1) line is given in Table 3. The broad line structures are extended

over a  $4.5' \times 5'$  region (the entire GRID map we observed) and elongated from northeast to southwest. Three maps of the blue wing (with a velocity range between  $-58$  and  $-38$   $\text{km s}^{-1}$ ), red wing (between  $-31$  and  $-27$   $\text{km s}^{-1}$ ), and the middle velocity, the broad line with the self-absorption (between  $-38$  and  $-31$   $\text{km s}^{-1}$ ) are shown in Figures 6 and 7. We chose these velocity ranges based on the CO(2-1) spectra in order to avoid materials that are not related to the shocked gas in the SNR G357.7+0.3. The CO spectra show two weak lines at the velocity  $-56$   $\text{km s}^{-1}$  and at  $-23$   $\text{km s}^{-1}$  (between  $-27$  to  $20$   $\text{km s}^{-1}$ ) on the top of the broad lines (see Figures 2 and 4) and the materials at these velocities are likely unrelated to the SNR. These features are less noticeable at higher transition lines of CO(4-3) and CO(3-2). The blue wing, the material moving toward us, is located in the south relative to the pre-shock gas (in green; this emission may include pre-shock gas) and the red wing, the material moving away from us, is located in the north as shown in Figure 7.

Figure 8 shows position-velocity maps that slice through the spectral data centered on BML-B (the center of IRS map) in R.A. and Decl direction, respectively. The exceptionally wide velocity dispersion of the broad molecular regions compared to the ambient gas (which has a typical width of  $<7$   $\text{km s}^{-1}$  FWHM; for example at  $\sim 0$   $\text{km s}^{-1}$ ) is evident. The map shows broad lines from  $-50$   $\text{km s}^{-1}$  to  $-10$   $\text{km s}^{-1}$  with an absorption dip at  $34$   $\text{km s}^{-1}$ . The broad line feature continues outside the map in R.A. direction.

We named three representative broad molecular line (BML) positions from the CO(2-1) grid spectra as BML-B, BML-C and BML-D in addition to the OH-A1 position (we call this position BML-A). The positions are marked in Figure 1 and listed in Table 2. BML-B is the peak of broad lines and has broader CO lines than the OH-A1(BML-A) and other positions. We note that the peak of the CO broad lines does not coincide with any of the OH positions as shown in Figure 1. We made ARO 12-m, *Spitzer* IRS, MOPRA, SOFIA, and additional APEX observations toward the BML-B position or its vicinity. The spectra of  $^{13}\text{CO}$ (1-0), CO(3-2) and HCO<sup>+</sup> toward BML-B, BML-C and BML-D are shown in Figure 9. CO(3-2) and HCO<sup>+</sup> spectra show broad lines with the widths of up to  $27$   $\text{km s}^{-1}$  from shocked gas (see Table 3) and  $^{13}\text{CO}$ (1-0) shows narrow components from cold gas. The HCO<sup>+</sup> taken with the 12-m telescope shows the broadest line with a  $\text{FWHM} = 27.96 \pm 0.02$   $\text{km s}^{-1}$  we detected as shown in Figure 9. The MOPRA spectrum also detects a broad line of HCO<sup>+</sup> as shown in Figure 10, although the signal-to-noise is not as good as that from the 12-m telescope. As we have seen in the position of OH-A1, the broad lines of CO or HCO<sup>+</sup> spectra show anti-correlation with  $^{13}\text{CO}$ (1-0). APEX spectra toward BML-B in Figure 11 show detections of CO(2-1) and  $^{13}\text{CO}$ (2-1). The lines are broad with widths of  $26$  and  $16$   $\text{km s}^{-1}$ , respectively (see Table 3). The line profiles also show self-absorption lines, but the  $^{13}\text{CO}$ (2-1) line shows only a very small amount of self-absorption. MOPRA additionally detects a broad line of HCN with a  $\text{FWHM}$  of  $\sim 25$   $\text{km s}^{-1}$ .

### 3.3. Self-absorption line in broad molecular line

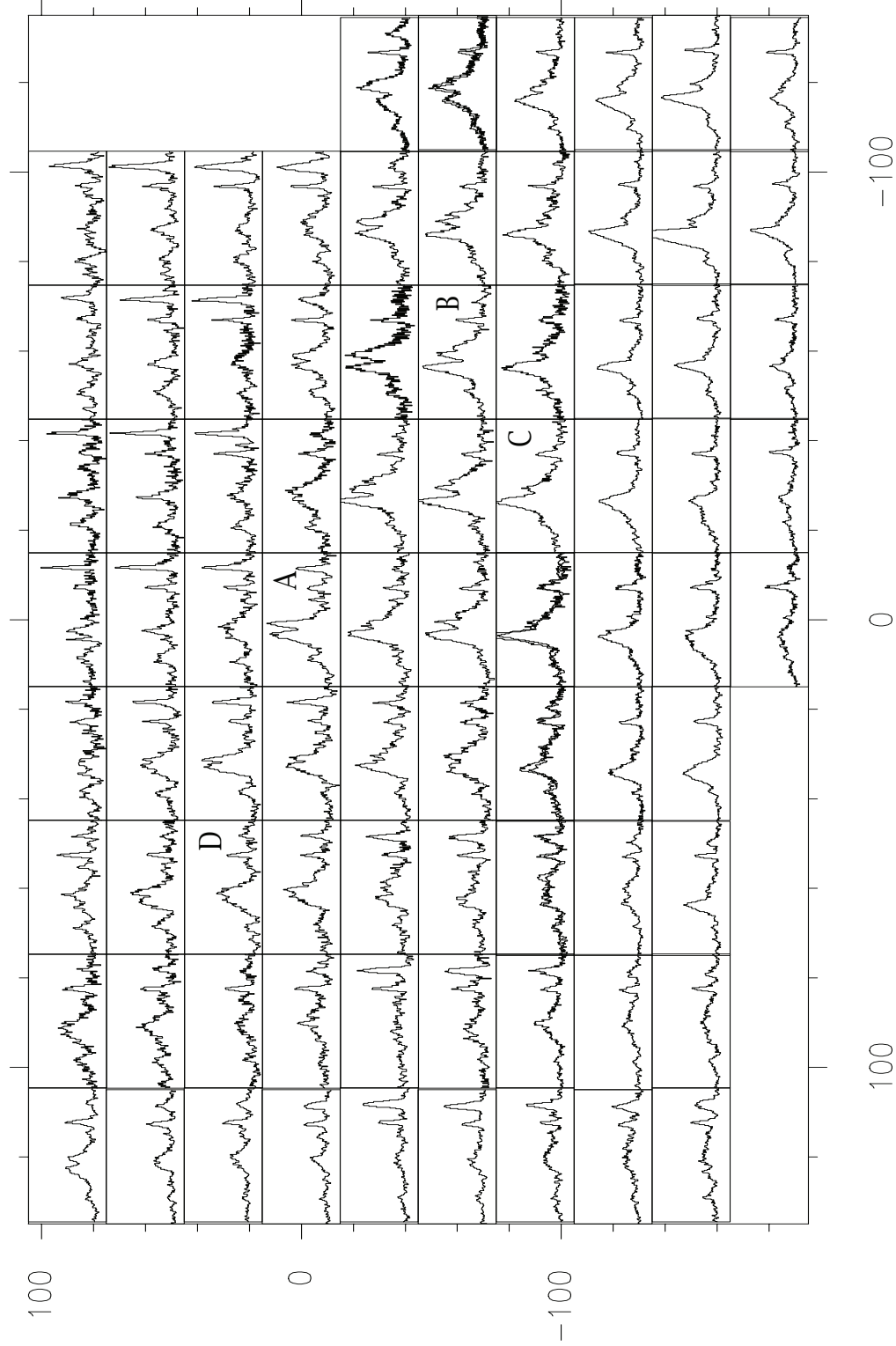


FIG. 5.— GRID spectra of CO (2-1) of G357.7+0.3 with a spacing of  $30''$  (units of x- and y-axis are offsets ( $''$ ) from the OH-A1 position). The BML-A, BML-B, BML-C and BML-D positions (see Table 2) with representative CO spectra are marked as A, B, C, and D, respectively. Broad lines appear in extended regions, and the structure shows elongated from northeast to southwest. The individual spectra have X-axis in velocity from  $-100$  to  $25 \text{ km s}^{-1}$  in velocity, and y-axis in temperature from  $-0.5$  to  $5.8$  in  $T_{mb}(\text{K})$ .

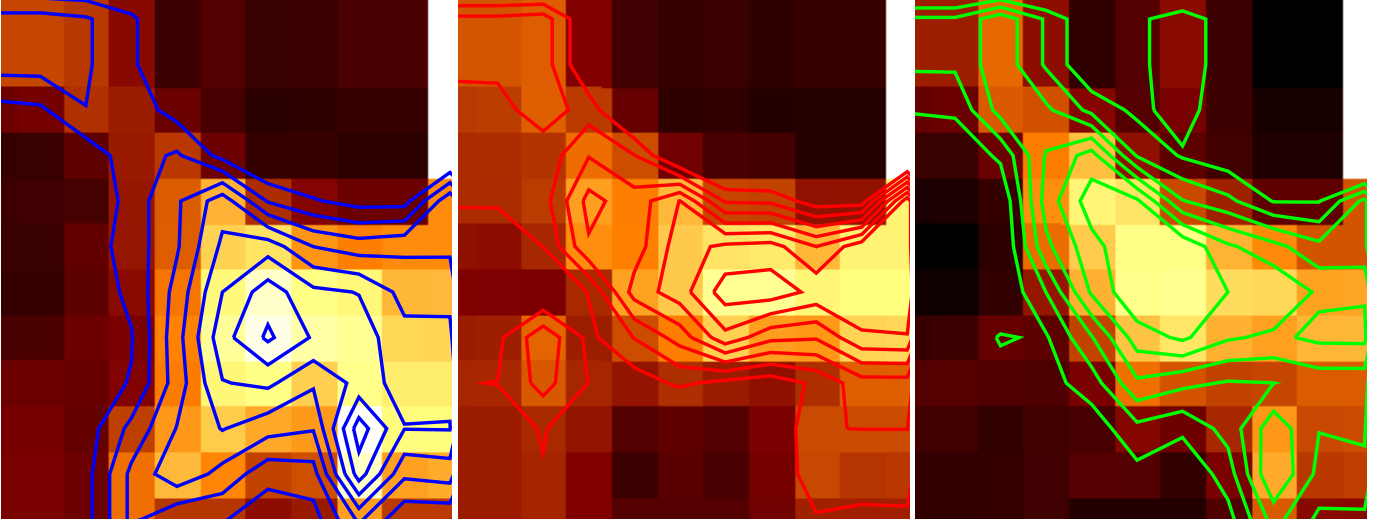


FIG. 6.— CO(2-1) broad line maps in three velocity ranges (R.A. and Decl. are labeled in Figure 7). Image of blue wing (left in blue contours) is from the velocity ranges between  $-53$  and  $-38$   $\text{km s}^{-1}$ , red wing image (middle; in red contours) between  $-31$  and  $-27$   $\text{km s}^{-1}$ , middle velocity image where the spectrum shows broad line with self-absorption (right; in green contours) is between  $-38$  and  $-31$   $\text{km s}^{-1}$ . Contours on blue wing image (left) are 13, 20.8, 28.7, 36.6, 44.4, 52.3, 20.14, and 68  $\text{K km s}^{-1}$ , on red wing image (middle) are 8, 10.5, 13.1, 15.7, 18.3, 20.8, 23.4, 23.4 and 26  $\text{K km s}^{-1}$ , and on the middle velocity map are 14, 17.8, 21.7, 25.5, 29.3, 33.3 and 37.0  $\text{K km s}^{-1}$ .

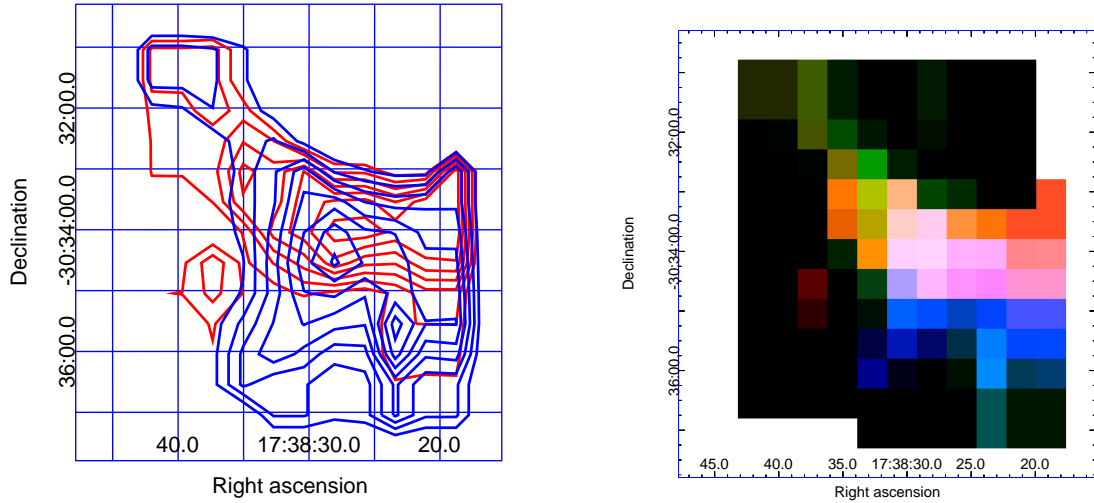


FIG. 7.— Comparison of blue and red wing images from CO(2-1) shown in Figure 6 (left). Three color images of three velocity range maps from the broad line shown in Figure 6; blue wing, red wing and middle velocity map are represented in blue, red and green, respectively (right).



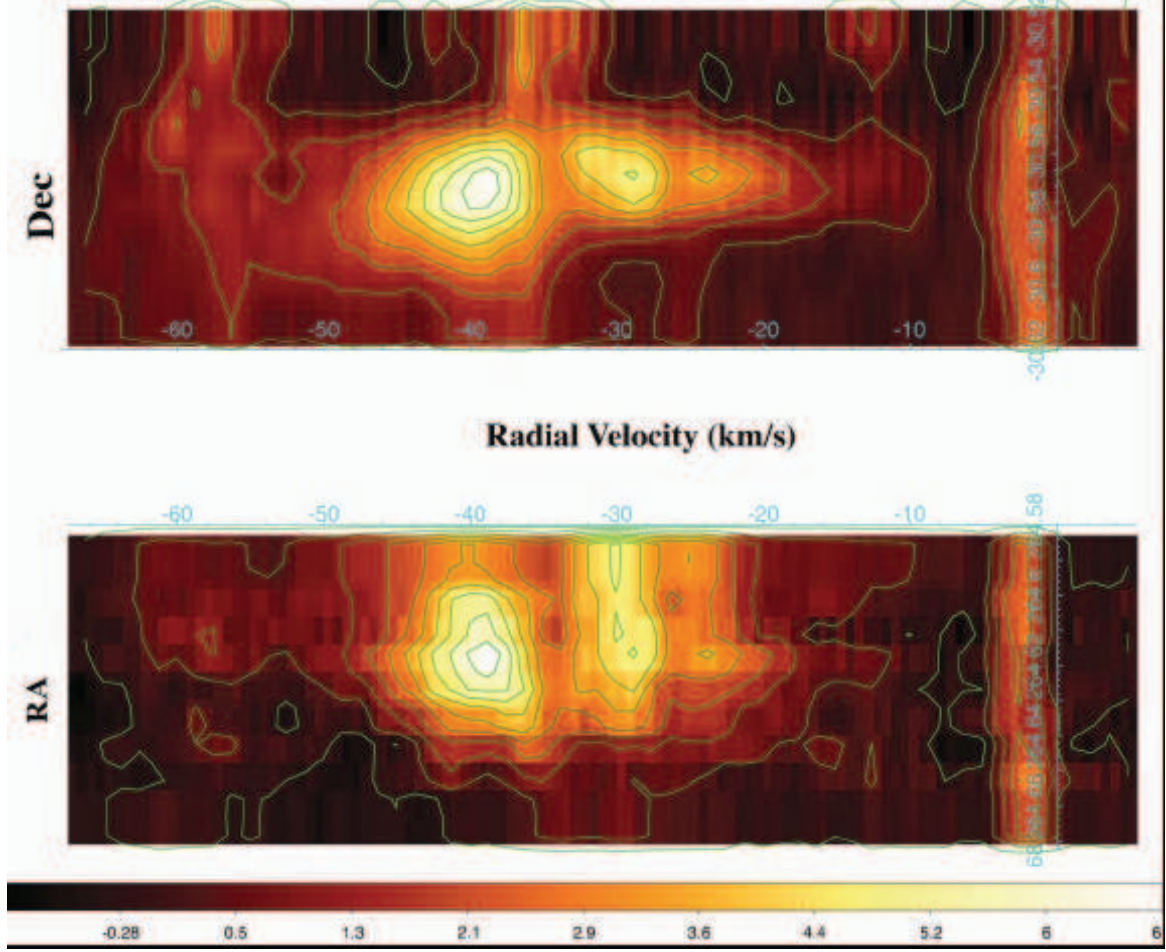


FIG. 8.— CO(2-1) position-velocity maps (a: top) cut at constant R.A. =  $17^{\text{h}}38^{\text{m}}26.9^{\text{s}}$  and (b: bottom) cut at constant decl =  $-30^{\circ}33'57.07''$ . Broad lines from  $-50 \text{ km s}^{-1}$  to  $-10 \text{ km s}^{-1}$  with an absorption dip at  $34 \text{ km s}^{-1}$ . The broad line feature continues outside the map in R.A. direction. Contours are 0.36, 1.07, 1.78, 2.49, 3.20, 3.91, 4.63, 5.45, 6.05 and  $6.76 \text{ K}$ . The positions are labeled in decimal degrees, for both (a) declination and (b) right ascension.

CO or  $\text{HCO}^+$  spectra toward BML-B, BML-C, and BML-D show similar anti-correlation of the broad lines of CO(3-2) and  $\text{HCO}^+$  with  $^{13}\text{CO}(1-0)$  as shown in Figure 9. In Table 2, the positions of B, C, and D are where CO(2-1) spectra reveal representative BMLs.

The narrow line components are unshocked clouds which are likely a part of parent molecular clouds of the shocked CO gas because they are approximately at the velocity similar to that of shocked gas. The line-of-sight absorption is stronger for the CO(2-1) transition, which can be absorbed by cold gas with substantial populations in the level  $J=1$ , than for the CO(3-2) or CO(4-3) transitions. In other words, the  $^{13}\text{CO}(1-0)$  emission, which traces the total column density and is dominated by the cold gas along the line of sight, matches very well the center and width of the apparent “notch” cut out of the  $^{12}\text{CO}$  spectra.

The optical depth of CO emission from low-lying energy levels of gas in quiescent molecular clouds is generally greater than unity. For  $\text{HCO}^+(1-0)$  the transition is out of the ground state, so even cold gas is readily detected in absorption. The precise correspondences between the  $^{13}\text{CO}$  emission and the apparent  $^{12}\text{CO}$  and  $\text{HCO}^+$  absorption notches indicate they are due to cold molecular gas in the parent molecular cloud. Conversely,

the *lack* of  $^{13}\text{CO}$  emission from the broader component that is so bright in  $^{12}\text{CO}$  indicates it is optically *thin* (see Section 4.3 for detailed discussion) and due to a smaller column density of more-highly-excited gas. A similar combination of broad emission with narrow superposed absorption lines was observed in the molecular-cloud-interacting SNRs W44 and W28 (Reach, Rho & Jarrett 2005). When there is bright emission from hot, shocked gas behind cold, unshocked gas, an absorption component appears. The  $^{12}\text{CO}(2-1)$  line also has narrow components at  $-57.9$ ,  $-13$ ,  $-1.8$  and  $13 \text{ km s}^{-1}$ ; these narrow components (line widths  $< 4 \text{ km s}^{-1}$ ) are from cold gas in other molecular clouds along the line of sight, unrelated to G357.7+0.3.

The narrow absorption line in the spectra of  $^{12}\text{CO}(4-3)$ ,  $^{12}\text{CO}(3-2)$ ,  $^{12}\text{CO}(2-1)$  and  $\text{HCO}^+$  is anti-correlated with  $^{13}\text{CO}(1-0)$  where the narrow line appears in emission (see Figures 2 and 4). The  $^{13}\text{CO}(3-2)$  line in Figure 4 shows a broad wing which is from shocked gas, and  $^{13}\text{CO}(1-0)$  shows a narrow line with a line width of  $3.9 \text{ km s}^{-1}$  which is pre-shocked gas. The  $^{13}\text{CO}(2-1)$  shows a combination of the two, a broad and narrow components. One gaussian component fit to  $^{13}\text{CO}(2-1)$  yielded a line width of  $7.5 \text{ km s}^{-1}$  as listed in Table 3. When we fit with two gaussian components, the fit yielded a broad component

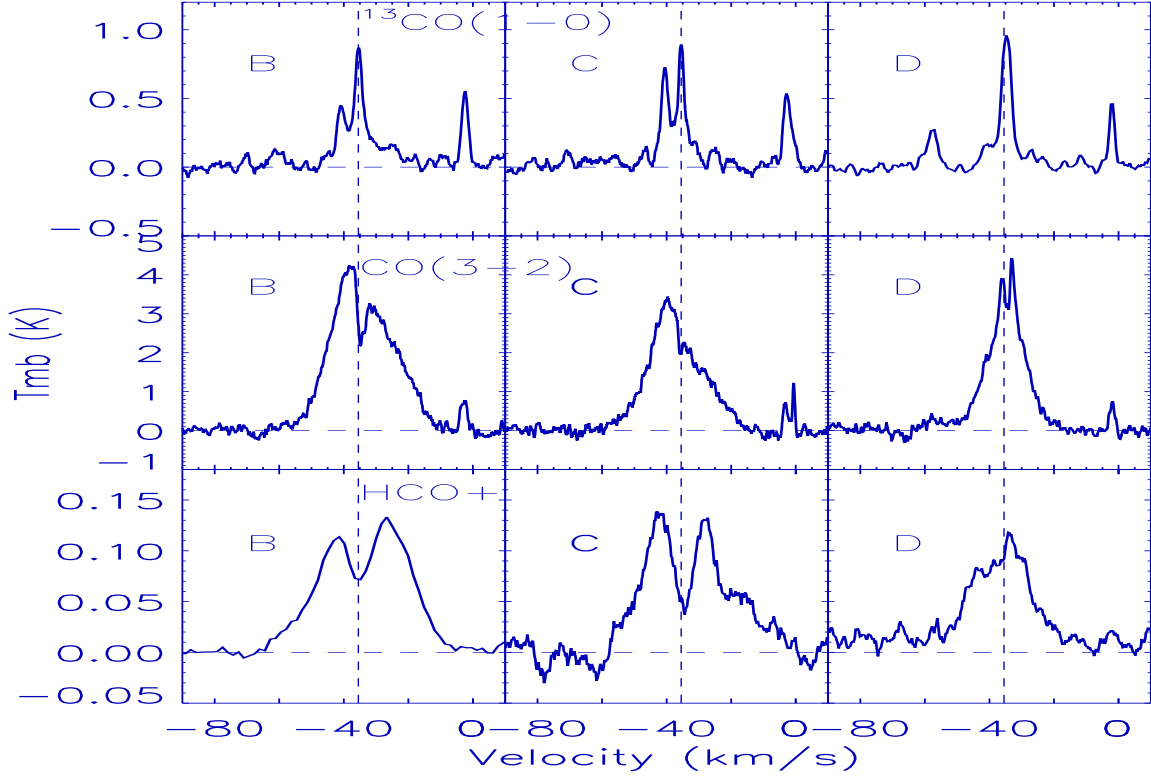


FIG. 9.— Comparison of  $^{13}\text{CO}(1-0)$ ,  $\text{CO}(3-2)$  and  $\text{HCO}^+$  spectra for the positions of BML-B, BML-C and BML-D.  $\text{CO}(3-2)$  data are taken with HHMT, and  $^{13}\text{CO}(1-0)$  and  $\text{HCO}^+$  data are taken with 12-m telescope.

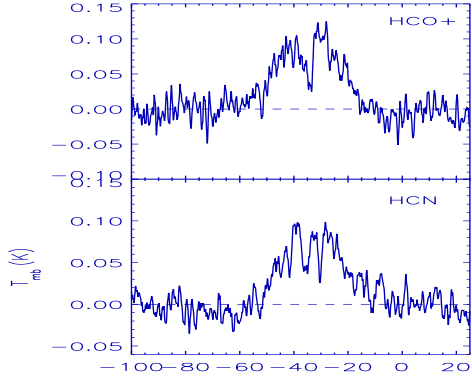


FIG. 10.— MOPRA spectra of  $\text{HCO}^+(1-0)$  and  $\text{HCN}(1-0)$  toward the position of BML-B.

with a width of  $8.57 \pm 0.43 \text{ km s}^{-1}$  and a narrow component with a width of  $2.22 \pm 0.14 \text{ km s}^{-1}$ . This is consistent with the idea that  $^{13}\text{CO}(2-1)$  shows a combination of pre-shock and post-shock CO emission.

#### 3.4. SOFIA GREAT spectra

In Figure 12 the SOFIA GREAT spectrum of  $[\text{C II}]$  at  $158 \mu\text{m}$  shows a broad line with a FWHM of  $15.7 \text{ km s}^{-1}$  (see Table 3). Although the detection is only  $3\sigma$ , the line profile and the FWHM of  $[\text{C II}]$  is similar to those of broad CO lines. The line strength is equivalent to  $2.84 \times 10^{-13} \text{ erg s}^{-1} \text{ cm}^{-2}$ . Using a beam size of  $14.1''$ , the surface brightness is  $7.85 \times 10^{-5} \text{ erg s}^{-1} \text{ cm}^{-2} \text{ sr}^{-1}$ . Ionic lines commonly originate from high veloc-

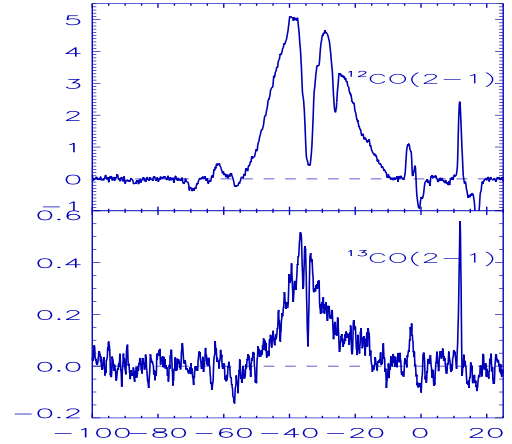


FIG. 11.— APEX spectra of  $^{12}\text{CO}(2-1)$  and  $^{13}\text{CO}(2-1)$  toward the position BML-B.

ity J-shocks (Hollenbach & McKee 1989; Rho et al. 2001; Reach & Rho 2000; Hewitt et al. 2009). A resolved  $[\text{O I}]$  spectrum of another SNR 3C391 at  $63 \mu\text{m}$  using ISO LWS shows a line width of  $100 \text{ km s}^{-1}$ . This indicates that atomic fine-structure lines such as  $[\text{O I}]$  and  $[\text{C II}]$  oxygen can originate from J-shocks. However, the line width of  $[\text{C II}]$  in G357.7+0.3 is small,  $15.7 \text{ km s}^{-1}$ , similar to the broad component of CO lines. This suggests that  $[\text{C II}]$  comes from the same shock responsible for the CO lines. In other words,  $[\text{C II}]$  is from a low ( $\sim 15 \text{ km s}^{-1}$ ) velocity shock. Draine, Roberge & Dalgarno (1983) show

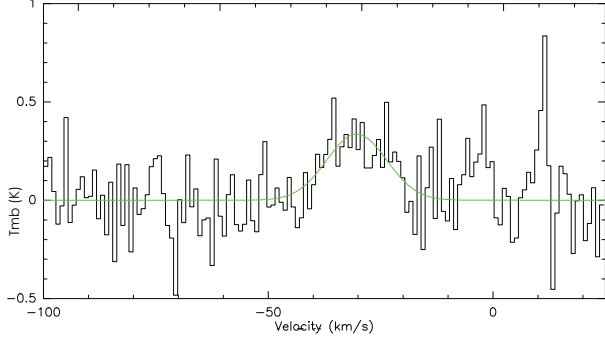


FIG. 12.— SOFIA GREAT spectrum of [C II] line is superposed on a gaussian fit. The width of the line is  $\Delta V = 16 \text{ km s}^{-1}$  and the line profile of [C II] is similar to those of CO lines.

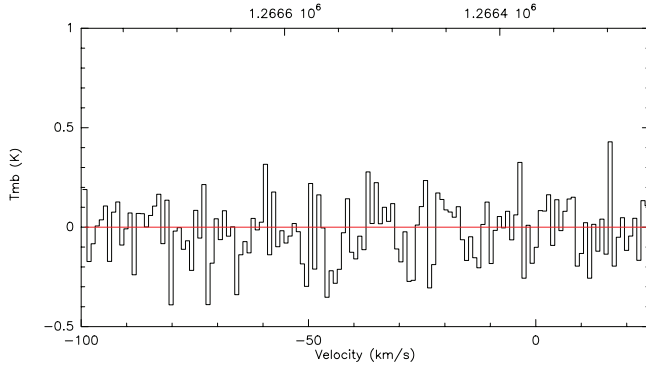


FIG. 13.— SOFIA GREAT spectrum of CO(11-10) line.

that ionic lines could be more important coolants than molecular lines even for low velocity ( $< 20 \text{ km s}^{-1}$ ) shock (see Figure 4 of Draine, Roberge & Dalgarno 1983). Unfortunately the models do not include [C II] at  $158 \mu\text{m}$  itself, so we cannot directly compare the line brightness of [C II] with the model. Non-quasi-steady model of CJ-shocks (introducing a J-type discontinuity in a C-type flow at a point in the steady-state profile that is located in downstream of the shock) show enhanced cooling by ions (e.g. oxygen) before molecular line cooling such as  $\text{H}_2$  and CO as described by Lesaffre et al. (2004a). These spectra may be the first direct evidence of such CJ shocks. The [C II] line is known to be an important cooling line in J-shock (Hollenbach & McKee 1989) and the detection of [C II] with the width of  $16 \text{ km s}^{-1}$  indicates that cooling by [C II] may be moderate in C-shock or CJ-shock in addition to cooling by various molecular lines (Kaufman & Neufeld 1996). The SOFIA spectrum of CO (11-10) line is not detected as shown in Figure 13 and its upper limit is  $0.14 \text{ K}$  which is a RMS noise estimated between  $-200$  to  $100 \text{ km s}^{-1}$ .

### 3.5. Molecular Cloud Maps Surrounding the SNR

We have mapped a large-scale molecular cloud structure surrounding the SNR G357.7+0.3 using  $^{13}\text{CO}(1-0)$  line that typically traces cold clouds. The spatial resolution of the map is  $47''$  and the map covers  $32' \times 32'$  larger than the size of SNR  $24' \times 24'$ .  $^{13}\text{CO}(1-0)$  image of

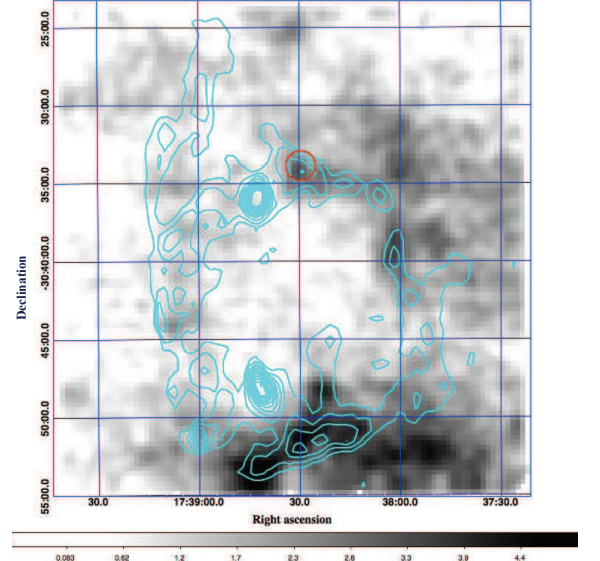


FIG. 14.—  $^{13}\text{CO}(1-0)$  image of G357.7+0.3 integrated over velocities  $-41$  to  $-31 \text{ km s}^{-1}$  (greyscale) obtained with the ARO 12-m telescope. The greyscale bar indicates the summed brightness in K; to convert to  $\text{K km s}^{-1}$ , multiplied by  $2.72 \text{ km s}^{-1}$ . Overlaid on the  $^{13}\text{CO}$  image are cyan-colored contours of the non-thermal radio brightness from the MOST Galactic Centre Survey (Gray 1994). The red circle indicates the location of the OH-A1 1720 MHz maser, where broad molecular lines are seen. The image is centered on R.A.  $17^{\text{h}}38^{\text{m}}31.9^{\text{s}}$  and Decl.  $-30^{\circ}39'19''$  (J2000) with a FOV of  $29.4' \times 30.1'$ .

G357.7+0.3 integrated over velocities  $-41$  to  $-31 \text{ km s}^{-1}$  obtained with the ARO 12-m telescope is shown in Figure 14. The supernova appears to be bounded by molecular gas, in particular its southern, western, and northwestern portions. The sharpness of the eastern radio continuum boundary in these contours is exaggerated because of taper of the MOST field of view.

Maps of  $^{13}\text{CO}$  emission toward SNR G357.7+0.3 integrated over 4 velocity ranges ( $+121 \pm 10$ ,  $+102 \pm 10$ ,  $+7 \pm 10$  and  $-31 \pm 10 \text{ km s}^{-1}$ ) are shown in Figure 15. Each panel is labeled in the top right with its velocity in red, with the location of peak as a red square. The blue contours repeated on each panel are the non-thermal radio brightness from the MOST Galactic Centre Survey (Gray 1994). Representative spectra from the locations of the bright peak of the 4 velocity maps (they are marked as squares in Figure 15) are shown in Figure 16. The 4 velocity components are likely at significantly different distance along the line of sight, but their kinematic distances cannot be inferred from the velocity and the galactic rotation curve, because the line of sight is so close to the Galactic center. The  $+7 \text{ km s}^{-1}$  component may be associated with the eastern boundary of the SNR but has not been shown to be associated. The supernova appears to be bounded by molecular gas in the  $-31 \text{ km s}^{-1}$  component, in particular its southern, western, and northwestern portions. The velocity of this component corresponds to that of the shocked gas and in particular the narrow self-absorption toward the broad CO. The red circle indicates the location of the OH 1720 MHz masers which are at  $-35$  to  $-37 \text{ km s}^{-1}$ . We already show broad molecular and carbon line detection in its northwestern portions, and possible extended



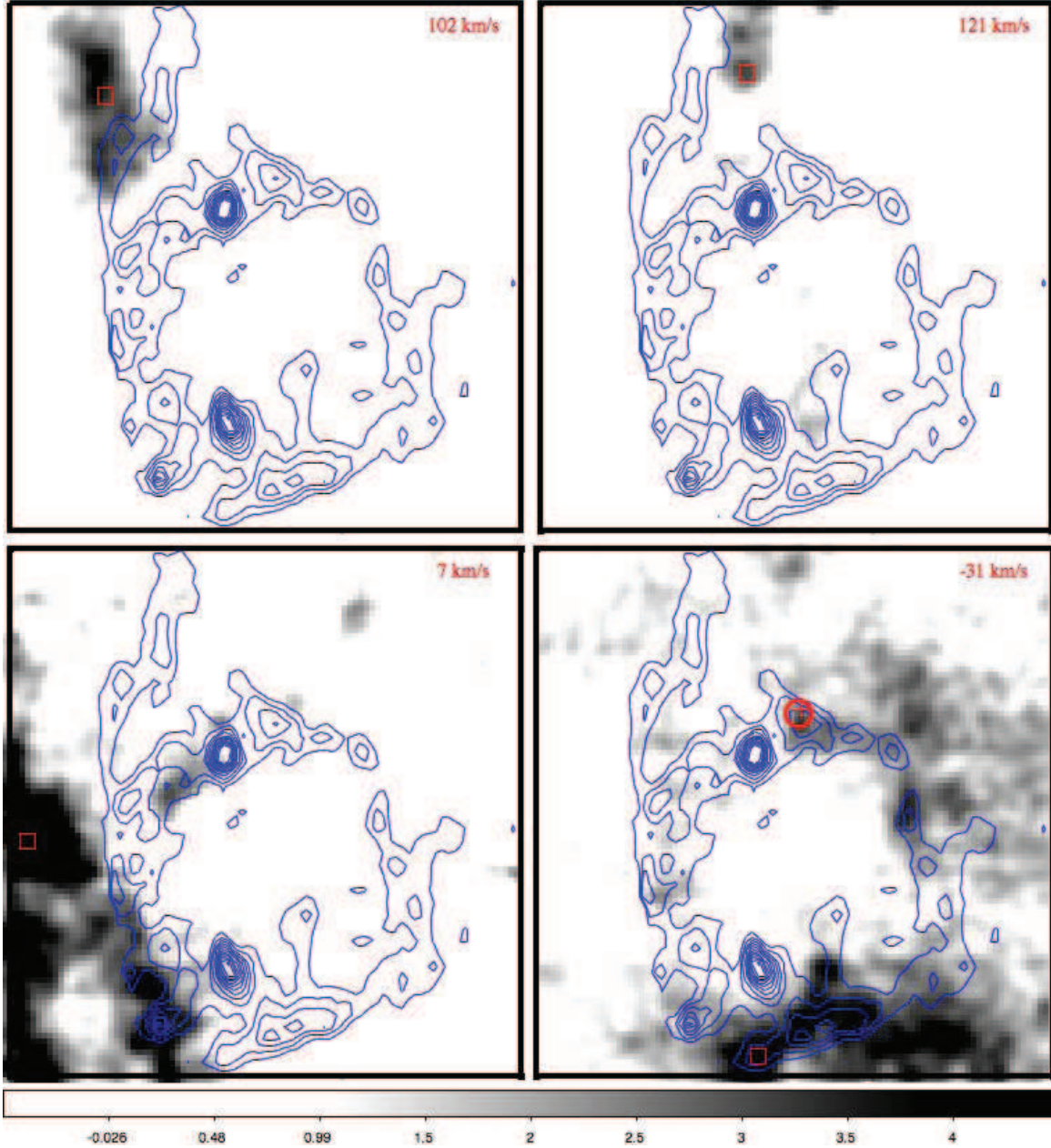


FIG. 15.— Maps of  $^{13}\text{CO}$  (1-0) emission toward the SNR G357.7+0.3 integrated over 4 velocity ranges. Each panel is labeled in the top right with its velocity in red, with the location of the highest intensity in each panel as a red square. The blue contours repeated on each panel are the non-thermal radio brightness. The area showing the broad  $^{12}\text{CO}$  lines toward the SNR is marked as a circle on the  $^{13}\text{CO}$  (1-0) map with  $-31 \text{ km s}^{-1}$ . The scale bar below the images for the greyscale  $^{13}\text{CO}$  images is in units of antenna temperature summed over channels; to convert to brightness temperature integrated over velocity ( $\text{K km s}^{-1}$ ), multiply by 2.3.

interaction sites may be found to western and southern portions.

### 3.6. Molecular Hydrogen with *Spitzer*

The *Spitzer* IRS spectrum where the broad CO emission from the SNR G357.7+0.3 is detected as shown in Figure 17. All rotational  $\text{H}_2$  lines within the IRS wavelength range are detected except S(6) line at  $6.109 \mu\text{m}$  (note the feature appeared around  $6.1 \mu\text{m}$  is a part of PAH emission and  $\text{H}_2$  S(6) line is not detected; for comparison with those in other SNRs, see Hewitt et al. 2011). The S(7) line is a weak detection. The detected  $\text{H}_2$  lines are S(0), S(1), S(2), S(3), S(4), S(5), and S(7) as listed in Table 4. Interestingly, G357.7+0.3

shows a significant lack of bright ionic lines compared with other SNRs which emit  $\text{H}_2$  emission (Andersen et al 2011; Hewitt et al. 2009; Neufeld et al. 2006). The only ionic line detected is weak [Si II] at  $34.8 \mu\text{m}$ .

The  $\text{H}_2$  maps at different wavelengths are shown in Figure 18. The  $\text{H}_2$  map at  $5.5 \mu\text{m}$  is too weak to see any structures, and the map at  $8 \mu\text{m}$  is blended with polycyclic aromatic hydrocarbon (PAH) features. The  $\text{H}_2$  maps show somewhat different structures from each other. This is also seen in other regions such as HH objects or other molecular interacting SNRs with shocked  $\text{H}_2$  emission (Neufeld et al. 2006, 2007). The  $\text{H}_2$  maps at  $6.9$  and  $9.6 \mu\text{m}$  (see Figures 18a and 18b) both show a northwestern rim along the CO blue wing emission and



TABLE 4  
OBSERVED LINE BRIGHTNESS IN THE *Spitzer* IRS SPECTRA

Wavelength ( $\mu\text{m}$ )	Line	FWHM ( $\mu\text{m}$ )	Line Brightness ( $\text{erg s}^{-1} \text{cm}^{-2} \text{sr}^{-1}$ )	De-reddened Brightness ( $\text{erg s}^{-1} \text{cm}^{-2} \text{sr}^{-1}$ )
$5.5004 \pm 0.0016$	H <sub>2</sub> S(7)	$0.056 \pm 0.004$	$2.29\text{E-}05 \pm 2.52\text{E-}06$	$3.39\text{E-}05 \pm 3.74\text{E-}06$
$6.9104 \pm 0.0006$	H <sub>2</sub> S(5)	$0.072 \pm 0.002$	$8.92\text{E-}05 \pm 2.44\text{E-}06$	$1.21\text{E-}04 \pm 3.30\text{E-}06$
$8.0037 \pm 0.0007$	H <sub>2</sub> S(4)	$0.061 \pm 0.002$	$3.52\text{E-}05 \pm 2.65\text{E-}06$	$6.11\text{E-}05 \pm 4.59\text{E-}06$
$9.6674 \pm 0.0003$	H <sub>2</sub> S(3)	$0.127 \pm 0.001$	$1.20\text{E-}04 \pm 9.82\text{E-}07$	$5.71\text{E-}04 \pm 4.65\text{E-}06$
$12.2821 \pm 0.0002$	H <sub>2</sub> S(2)	$0.082 \pm 0.001$	$6.13\text{E-}05 \pm 1.60\text{E-}06$	$1.14\text{E-}04 \pm 2.97\text{E-}06$
$17.0310 \pm 0.0002$	H <sub>2</sub> S(1)	$0.164 \pm 0.001$	$2.04\text{E-}04 \pm 8.03\text{E-}07$	$3.46\text{E-}04 \pm 1.36\text{E-}06$
$28.1932 \pm 0.0012$	H <sub>2</sub> S(0)	$0.299 \pm 0.003$	$3.08\text{E-}05 \pm 3.14\text{E-}07$	$4.19\text{E-}05 \pm 4.28\text{E-}07$
$34.8466 \pm 0.0037$	[Si II]	$0.196 \pm 0.009$	$3.19\text{E-}05 \pm 2.66\text{E-}06$	$4.04\text{E-}05 \pm 3.37\text{E-}06$

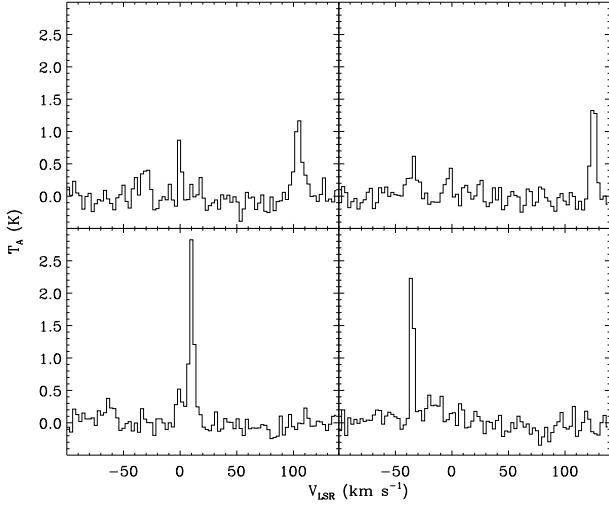


FIG. 16.— Representative  $^{13}\text{CO}(1-0)$  spectra of 4 velocity channel maps in Figure 15. The extracted regions are marked as boxes located in the northeast on the  $+102 \text{ km s}^{-1}$  velocity map, in the north on the  $+121 \text{ km s}^{-1}$ , in the east on the  $7 \text{ km s}^{-1}$  map, and in the southern region on the  $-31 \text{ km s}^{-1}$  map.

other H<sub>2</sub> maps at 12.2, 17 and  $28\mu\text{m}$  (see Figures 18c, 18d and 18e) show elongated emission in the east-west direction, around the CO peaks of red wing emission. The H<sub>2</sub> maps show a concentration of emission at the peak of CO broad emission. However, because of different spatial resolution between H<sub>2</sub> (3-6'') and CO maps (beam size of 3'' vs. 22''), detailed structure could not be compared. The one-to-one correspondence between H<sub>2</sub> emission and broad CO emission is observed in IC 443 (see Rho et al. 2001). H<sub>2</sub> emission from G357.7+0.3 is probably collisionally excited from a shock, but we can not rule out contribution from UV pumping. Near-IR observations of vibrational H<sub>2</sub> lines are required to determine if there is contribution from UV pumping. High resolution CO images such as using ALMA could produce CO maps with a high spatial resolution comparable to or greater than those of H<sub>2</sub> images.

We have examined *Spitzer* IRAC and MIPS images (aorkey of 14296832 and 14658560), and we did not find any emission associated with the SNR. IRAC band 2 emission includes bright H<sub>2</sub> lines and shows shocked H<sub>2</sub> emission for many SNRs as shown in the GLIMPSE survey (Reach et al. 2006). When we carefully examined IRAC band 2 emission, we note that the background emission ( $6-7 \text{ MJy sr}^{-1}$ ) is a factor of 2-3 higher than those in other SNRs. The reason is likely because the

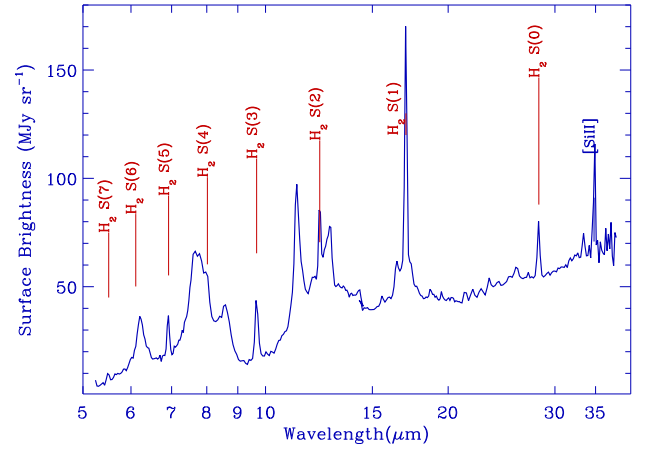


FIG. 17.— *Spitzer* IRS spectrum of G357.7+0.3 showing strong H<sub>2</sub> but lacking ionic lines (only [Si II] is shown).

background emission near the Galactic Center is high.

PAH emission appears in the spectrum of G357.7+0.3 shown in Figure 17. However, it is unclear if PAH emission belongs to the SNR or not because the area covered by the IRS observations seem to be mostly inside the SNR, except possibly for the SL1. We examined H<sub>2</sub> map at  $9.6\mu\text{m}$  where the northern part of IRS image may cover outside the SNR (see Figure 18b; note the boundary of the shock front is unclear because of lack of high resolution images). When we assume the emission in the northern part is background, the PAH emission disappeared. When we examined mosaicked post-calibrated image (pbcd), we don't see much variation of PAH emission. Many middle-aged SNRs show PAH emission as noted by Andersen et al (2011). However, because the SNR is large compared to the area we covered, future observations to cover a larger area including the area outside the SNR are necessary to confirm or disprove that PAH emission doesn't belong to the SNR G357.7+0.3.

We estimated the extinction value by using the silicate absorption dip around  $10\mu\text{m}$  using PAHFIT (Smith et al. 2007). The fit yielded a value of optical depth at  $9.7\mu\text{m}$ ,  $\tau(9.7\mu\text{m})$ , of 0.47, which is equivalent to an extinction value of  $A_v = 8.3 \text{ mag}$  using an averaged value of  $A_v/\tau(9.7) = 18.5 \pm 2.0$  from observed values (Draine 2003). This is equivalent to the line of sight column of  $N_H = 1.5 \times 10^{22} \text{ cm}^{-2}$ . This estimate is comparable to the value by Leahy (1989) assuming an average value of  $3 \times 10^{21} \text{ cm}^{-2}$  per kpc. The column density of

G357.7+0.3 in the line of sight is comparable to that of W44 (Rho et al. 1994).

#### 4. DISCUSSION

##### 4.1. Excitation of Molecular Hydrogen

The set of detected rotational  $\text{H}_2$  lines in Table 4 is an excellent diagnostic of physical conditions in the shocked gas of G357.7+0.3. An excitation diagram of the rotational  $\text{H}_2$  lines was presented by Hewitt et al. (2009). An excitation diagram from the de-reddened brightnesses of  $\text{H}_2$  lines is presented in Figure 19. We have fit the data using a model of two-temperature local-thermal equilibrium (LTE). The two-temperature fit yields a warm temperature ( $T_{\text{warm}}$ ) of 197 K with a column density ( $N_{\text{warm}}$ ) of  $2.3 \times 10^{21} \text{ cm}^{-2}$  and an ortho-to-para ratio (OPR) of 2.1, and a high temperature ( $T_{\text{hot}}$ ) of 663 K with a column density ( $N_{\text{hot}}$ ) of  $2.7 \times 10^{19} \text{ cm}^{-2}$  and an OPR of 3.

The warm temperature (197 K) component shows an OPR of 2, indicating the emission has not reached an equilibrium OPR. Conversion of para-to ortho- $\text{H}_2$  behind the shock depends on collisions with atomic hydrogen and is inefficient at low temperature due to the energy barrier ( $E/k \sim 4000$ ) in that conversion. Neufeld et al. (2006) suggested that the non-equilibrium  $\text{H}_2$  OPRs were consistent with shock models in which the gas is warm for a time period shorter than that required for reactive collisions between H and para- $\text{H}_2$  to establish an equilibrium OPR. Hewitt et al. (2009) show detection of  $\text{H}_2$  from six SNRs and the  $\text{H}_2$  emission has a warm component with  $T_w \sim 250 - 550 \text{ K}$  and a column density of  $\sim 10^{20} \text{ cm}^{-2}$ , and a hot component with  $T_h \sim 1000 - 2000 \text{ K}$  and a column  $N_w \sim 10^{19} \text{ cm}^{-2}$ . IC 443 shows a higher, warm temperature of 627 K (Neufeld et al. 2007) while G357.7+0.3 shows a lower value 197 K for a warm temperature. There are differences between SNRs, and non-LTE model may help to distinguish their difference in physical conditions as the  $\text{H}_2$  fitting is done with a simplified LTE model,  $\text{H}_2$  S(7) line at  $5.5 \mu\text{m}$  in G357.7+0.3 is above the two-temperature model, indicating there may be a third (hotter,  $>1000 \text{ K}$ ) component present as other molecular SNRs show such hot temperature components (Hewitt et al. 2009; Richter, Graham & Write 1995; Neufeld et al. 2007). However, the S(7) line in G357.7+0.3 is relatively weak compared with those in other molecular SNRs. Near-infrared follow-up observations of  $\text{H}_2$  lines combined with our *Spitzer* rotational lines and non-LTE model may be required to identify differences of physical condition of  $\text{H}_2$  in G357.7+0.3. Nevertheless, we find a difference in the best-fitted shock model in G357.7+0.3 from those of other molecular SNRs as described below.

##### 4.2. Implication of Shock Models from Molecular Hydrogen

We compare several shock models with the observed  $\text{H}_2$  emission. We use published models; C-shocks are from Le Boulton et al. (2002), which was applied to Orion and Wilgenbus et al. (2000), and J-shock models are from Hollenbach & McKee (1989). We use a grid of shock models and the  $\text{H}_2$  excitation was fitted using least squares fitting; detailed methods were described in Hewitt et al. (2009). A grid of computed C-shock models

TABLE 5  
SUMMARY OF SHOCK MODEL FITTING BASED ON  $\text{H}_2$  DATA

Model	$\Delta\chi^2$	density ( $\text{cm}^{-3}$ )	velocity ( $\text{km s}^{-1}$ )	OPR
One C-shock	800	$n=10^3$	30	3
<b>Two C-shock</b>	<b>17</b>	<b><math>n=10^4</math></b>	<b>30 (or 10)</b>	<b>2</b>
		<b><math>n=10^5</math></b>	<b>10</b>	–
C-shock	148	$n=10^3$	10	–
+ J-shock		$n=10^5$	5	3
C-shock	300	$n=10^3$	20	–
+ J-shock		$n=10^6$	150	–

spans ( $\log_{10} n_0$ ) = 3, 4, 5, 6  $\text{cm}^{-3}$ ,  $v_s$  = 10, 15, 20, 25, 30, 40  $\text{km s}^{-1}$ , and OPR = 0.01, 1, 2, 3. A grid of J-shock models are with densities of  $10^3, 10^4, 10^5, 10^6 \text{ cm}^{-3}$  and shock velocities of 30-150  $\text{km s}^{-1}$  in 10  $\text{km s}^{-1}$  increments. The fitted results are shown in Figure 20 and are summarized in Table 5. The two C-shock model yielded the best model over one component shock model or a combination of C-shock and J-shock models. The best fit is a combination of two slow C-shock models; a C-shock model with a density of  $10^4 \text{ cm}^{-3}$  and a velocity of 10  $\text{km s}^{-1}$ , and a second component of C-shock with a density of  $10^5 \text{ cm}^{-3}$  and the same velocity of 10  $\text{km s}^{-1}$ . The errors of the estimated density, shock velocity and OPR are limited to the available grid of the shock models.

Other molecular SNRs generated an equivalent quality of the fitting between a model of two C-shocks and a combination of C- and J-shock models (e.g. Hewitt et al. 2009). In contrast, G357.7+0.3 strongly favors the two C-shock model over a combination of C- and J-shocks based on  $\text{H}_2$  model fitting. G357.7+0.3 also lacks ionic lines in the IRS spectra; again in contrast to other molecular SNRs shown in Andersen et al (2011) and Neufeld et al. (2007). Most importantly, the detection of [C II] using SOFIA GREAT shows the FWHM is only 16  $\text{km s}^{-1}$  comparable to those of millimeter CO lines. All these facts show evidence of C-shocks and against the presence of J-shocks. This is in contrast to the results in the SNR G349.7+0.2 which shows the presence of J-shocks by showing a large line width ( $\sim 150 \text{ km s}^{-1}$ ) of a molecular water line (Rho et al. 2015).

##### 4.3. Line Opacity of the CO Molecular Gas

We use two pairs of  $^{12}\text{CO}$  and  $^{13}\text{CO}$  lines to estimate line opacities of CO. The first pair is  $^{12}\text{CO}(3-2)$  and  $^{13}\text{CO}(3-2)$  lines and the second pair is  $^{12}\text{CO}(2-1)$  and  $^{13}\text{CO}(2-1)$  lines. The ratio of  $^{12}\text{CO}(3-2)$  and  $^{13}\text{CO}(3-2)$  line intensities of the broad line is 17-40 where the ratio varies depending on the velocity. The broad line is defined as the lines at the velocity between -58 and -38  $\text{km s}^{-1}$  (blue CO wing), and at the velocity between -31 and -27  $\text{km s}^{-1}$  (red CO wing), and excludes the velocity range with the self-absorption. The ratio between  $^{12}\text{CO}(2-1)$  and  $^{13}\text{CO}(2-1)$  is almost the same as the ratio between  $^{12}\text{CO}(3-2)$  and  $^{13}\text{CO}(3-2)$  lines.

The ratio of the  $^{12}\text{CO}/^{13}\text{CO}$  lines is related to the optical depth of the  $^{12}\text{CO}$  line,  $\tau$ , and the abundance ratio,  $X$ , of  $^{12}\text{CO}$  over  $^{13}\text{CO}$ :

$$\frac{T_{12}}{T_{13}} = \frac{1 - e^{-\tau_{12}}}{1 - e^{-\tau_{13}}} = \frac{1 - e^{-\tau_{12}}}{1 - e^{-\tau_{12}/X}} \quad (1)$$

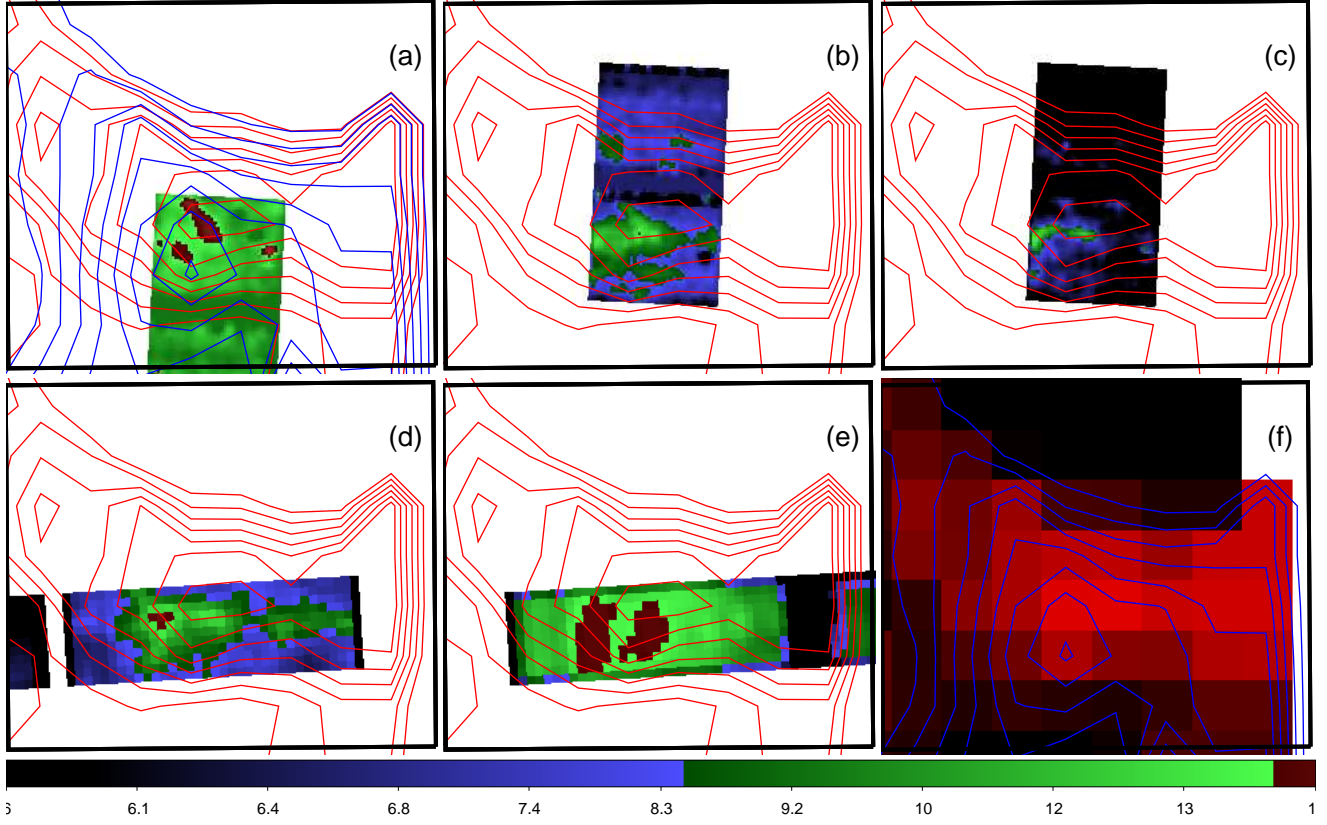


FIG. 18.—  $\text{H}_2$  maps of G357.7+0.3 at (a) S(5) at  $6.9\mu\text{m}$ , (b) S(3) at  $9.6\mu\text{m}$ , (c) S(2) at  $12.2\mu\text{m}$ , (d) S(1) at  $17\mu\text{m}$ , (e) S(0) at  $28\mu\text{m}$ , and (f) CO(2-1) red wing of broad line image (in red) superposed on blue wing contours. The region covered and contours is the same as in Figure 7. The colorbar applies to panels (a)-(e) and the labeled numbers apply to only panel (d) in units of  $\text{MJy sr}^{-1}$ . The FOV of the images is  $4.3' \times 3'$  centered on R.A.  $17^{\text{h}}38^{\text{m}}28^{\text{s}}$  and Dec.  $-30^\circ 34'00''$ .

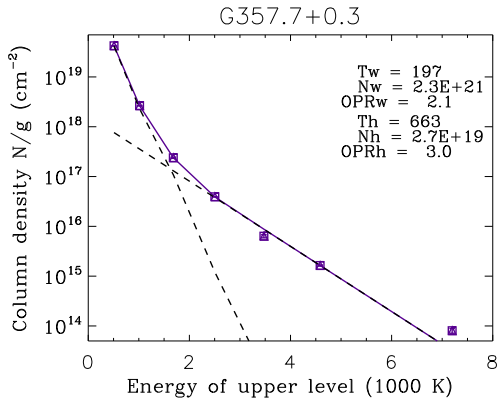


FIG. 19.—  $\text{H}_2$  excitation diagram of G357.7+0.3. The IRS data are marked as squares. The fitting results of two-temperature LTE fit are shown.

We solved  $\tau_{12}$  iteratively based on the observed ratio of  $T_{12}/T_{13}$  and we adopted  $X = 60$  (Lucas & Liszt 1998). From the observed line ratio (17-40) of the broad lines, the optical depth is in the range 0.9-3.6, which we observed is optically thin or slightly optically thick gas.

We estimate the optical depth of the apparent absorption in the  $^{12}\text{CO}$  lines (at the velocity between  $-38$  and  $-31 \text{ km s}^{-1}$ ). Estimating the center of the apparent absorption dip in intensity as a factor of 3-17, the optical depth is 3.6-25. The cloud includes optically thick gas which is the portion of the cold gas located in front of the warm, shocked gas. The optical depth of CO is esti-

mated for the molecular clouds at velocities of  $13 \text{ km s}^{-1}$  in Figures 2 and 8. The ratio of the line brightnesses  $^{12}\text{CO}/^{13}\text{CO}$  at  $13 \text{ km s}^{-1}$  is  $\sim 5$ , which corresponds to the optical depth of 13. The clouds at  $13 \text{ km s}^{-1}$  are optically thick from unshocked gas and are not related to the SNR G357.7+0.3.

#### 4.4. Large Velocity Gradient Analysis of the CO Molecular Gas

Using the three observed line brightnesses of  $^{12}\text{CO}(2-1)$ ,  $^{12}\text{CO}(3-2)$  and  $^{12}\text{CO}(4-3)$  in Table 3, we constrain the physical conditions in the shocked CO gas. An average value between APEX and HHSMT line intensities for the same line is used. We have made non-LTE analysis using RADEX (van der Tak et al. 2007), which is a radiative transfer code at the intermediate level; the most advanced methods that drop the local approximation and solve for the intensities (or the radiative rates) as functions of depth into the cloud, as well as of velocity. We use an average velocity width of  $17.3 \text{ km s}^{-1}$ , and the line brightnesses calculated from the averages of the measured line integrals divided by the line widths from Table 3. We assume that the emission is uniform on the scale of the largest beam of  $30''$ . Note that we don't have spatial information on scales smaller than  $30''$  because we only have one spectrum for each line except CO(2-1) and the beam size of CO(2-1) is  $30''$ . Using the RADEX model, confidence contours of a  $\text{H}_2$  volume den-

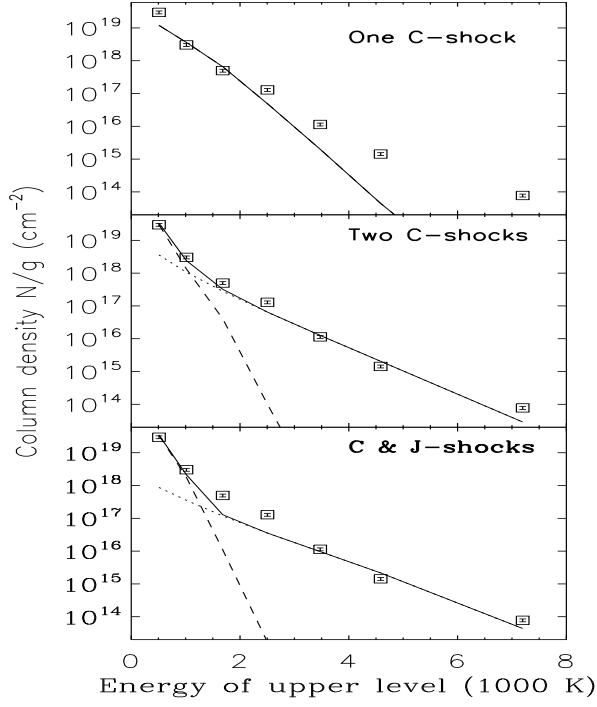


FIG. 20.— Comparison of fitted shock models to excitation of  $\text{H}_2$ . The data are shown with errors. From top to bottom, a single C-shock, two C-shocks and a combination of one C-shock and one J-shock. The best fit results are listed in Table 5. In cases of multiple-shocks, the slower shock is plotted with a dashed line and the faster shock with a dotted line. The total contribution of the two shock components is plotted as a solid line.

sity density  $[n(\text{H}_2)]$ , CO column density  $[N(\text{CO})]$ , and gas kinetic temperature  $[T]$  are obtained as shown in Figure 21. The best fit yields  $n(\text{H}_2) = 1.7^{+0.8}_{-0.5} \times 10^4 \text{ cm}^{-3}$ ,  $N(\text{CO}) = 5.6^{+0.1}_{-0.1} \times 10^{16} \text{ cm}^{-2}$ , and  $T = 75^{+30}_{-15} \text{ K}$ . The temperature inferred from the CO lines is roughly comparable to the ‘warm’  $\text{H}_2$  emission traced by the low-J  $\text{H}_2$  rotational lines; if these gases are from the same material, then the abundance of  $[\text{CO}/\text{H}_2]$  is  $2.4 \times 10^{-5}$ . That abundance is only 5% of the maximum CO abundance that would occur if all C and most O were locked into CO molecules ( $5 \times 10^{-4}$ ), which means much of the C is likely in atomic gas (as  $\text{C}^+$ ) or solids (contributing to the infrared continuum). Combining the volume density inferred from the CO excitation with the  $\text{H}_2$  column density from the  $\text{H}_2$  line brightness, the emitting region is  $0.04 \pm 0.02 \text{ pc}$  along the line of sight. This short path length corresponds to  $1''$  on the sky, which is smaller than the resolutions of the telescopes, despite the source appearing extended. When we examine the  $\text{H}_2$  image at  $6.9 \mu\text{m}$  (which has the highest spatial resolution in all  $\text{H}_2$  images) as shown in Figure 18, the size of the smallest knot is about  $3''$ . This is the limit of spatial resolution of the IRAC image. Thus, the  $1''$  structures were not resolved by our  $\text{H}_2$  images. The likely geometry of the emitting region is thin sheets, which are the post-shock regions with shock fronts spanning regions large than the beam.

Figure 22 shows the CO surface brightness as a function of upper rotation level ( $J_{\text{upper}}$ ) of CO. The best fit model is shown as a dotted line. The upper limit of SOFIA CO(11-10) line is above the brightness from the

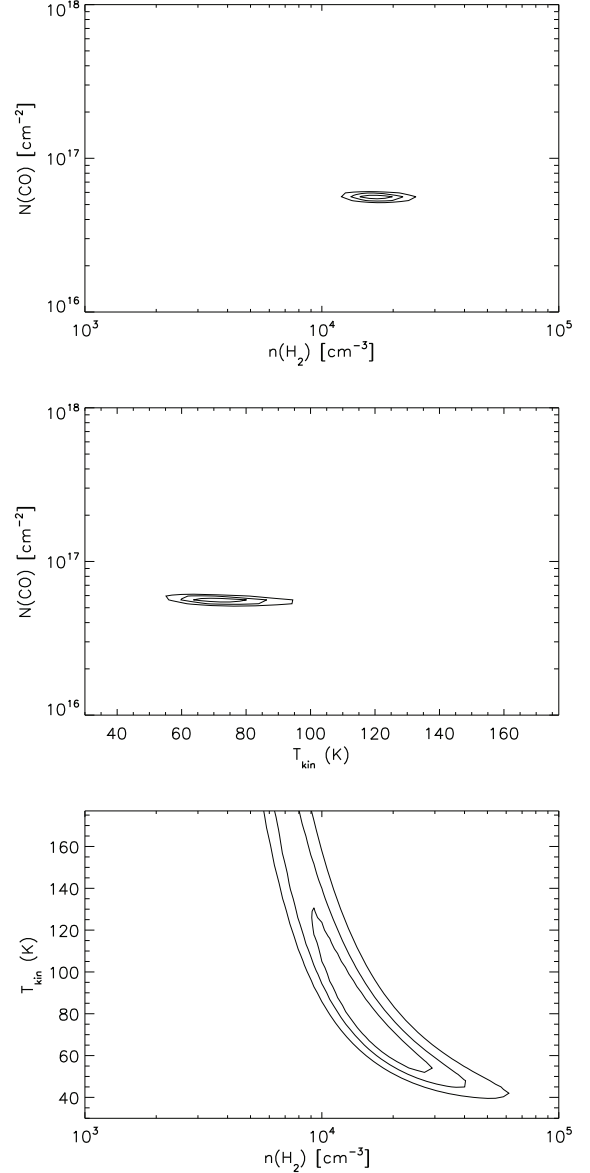


FIG. 21.— Comparison of the CO line brightness to RADEX models at different  $\text{H}_2$  density,  $n(\text{H}_2)$ , CO column density,  $N(\text{CO})$ , and gas temperature,  $T$ . The contours are the goodness-of-fit,  $\chi^2$ , for models compared to all three line brightnesses; contours are 99%, 90% and 67% confidence intervals.

model and the model indicates that a longer observation with SOFIA GREAT would have detected the line (note that the integration time of CO(11-10) was just 5 minutes). The volume density,  $n(\text{H}_2)$ , or the emitting CO gas in G357.7+0.3 is lower than those of a few SNRs (which includes a density of  $10^6 \text{ cm}^{-3}$ ) (for example Hewitt et al. 2009), but comparable to that of W28 (Neufeld et al. 2014).

The critical density of CO(4-3) is  $3.2 \times 10^4$  ( $3.7 \times 10^4$ ,  $2.4 \times 10^4$ )  $\text{cm}^{-3}$  for 200 K (30, 3000 K), and CO(3-2) is  $1.03 \times 10^4$  ( $1.1 \times 10^4$ ,  $8.6 \times 10^3$ )  $\text{cm}^{-3}$  for 200 K (30, 3000 K), and CO(2-1) is  $2.04 \times 10^3$  ( $2.2 \times 10^3$ ,  $1.9 \times 10^3$ )  $\text{cm}^{-3}$  for 200 K (30, 3000 K), respectively. Because the critical density of CO is low, CO is often used as a thermometer of the ISM. The volume density derived by a



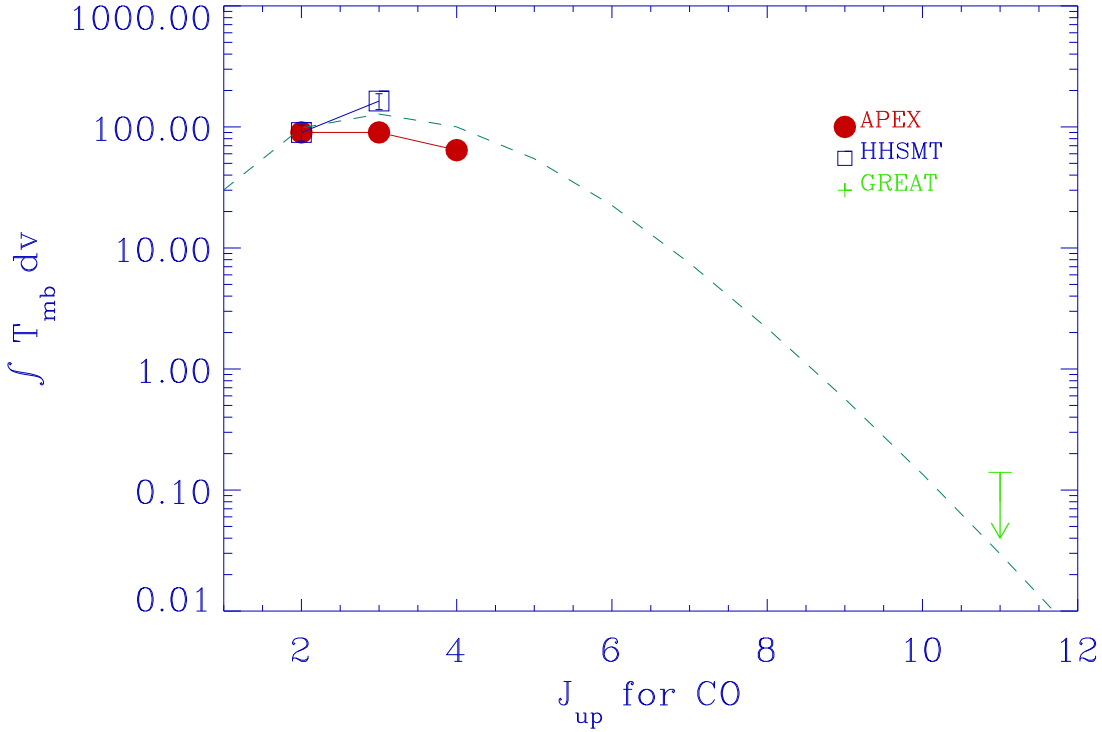


FIG. 22.— CO surface brightness diagram as a function of  $J_{up}$  with HHSMT and APEX observations. The upper limit of SOFIA GREAT (green arrow) is shown. The best-fit of RADEX model is shown in a dotted line (dark green).

RADEX model is slightly lower than the critical densities of CO(4-3) and CO(3-2) and higher than that of CO(2-1). Shocked gas of CO(2-1) is collisionally dominated while the CO gas emitting CO (4-3) and CO(3-2) is partially subthermal.

## 5. CONCLUSION

1. From the relatively unknown SNR G357.7+0.3, we discover broad molecular lines of CO(2-1), CO(3-2), CO(4-3),  $^{13}\text{CO}$  (2-1) and  $^{13}\text{CO}$  (3-2),  $\text{HCO}^+$  and HCN using the HHSMT, 12-Meter Telescope, APEX and MOPRA telescopes. The widths of the broad lines are 15-30  $\text{km s}^{-1}$ , that are caused by strong supernova (SN) shocks passing through dense molecular clouds. The detection of such broad lines is unambiguous, direct evidence of shocked gas. This is the first evidence showing that G357.7+0.3 is a SNR interacting with molecular clouds.

2. We present detection of shocked molecular hydrogen ( $\text{H}_2$ ) in the mid-infrared using the *Spitzer* IRS observations. The observations covered an area of about  $1'$  with short-low and  $\sim 3' \times 1'$  with long-low. The rotational  $\text{H}_2$  lines of S(0)-S(5), and S(7) with the IRS are detected. The detection of  $\text{H}_2$  lines is also evidence that G357.7+0.3 is interacting with molecular clouds. The two-temperature LTE fit yields a warm temperature ( $T_{\text{warm}}$ ) of 197 K with a column density ( $N_{\text{warm}}$ ) of  $2.3 \times 10^{21} \text{ cm}^{-2}$  and an ortho-to-para ratio (OPR) of 2.1, and a high temperature ( $T_{\text{hot}}$ ) of 663 K with a column density ( $N_{\text{hot}}$ ) of  $2.7 \times 10^{19} \text{ cm}^{-2}$  and an OPR of 3. The ortho-to-para ratio of the low temperature component is less than 3, indicating that the SNR G357.7+0.3

is propagating into cold quiescent clouds.

4. We observed [C II] at  $158 \mu\text{m}$  and high-J CO(11-10) observations with the GREAT on board SOFIA. CO(11-10) is not detected, but GREAT spectrum of [C II] shows a  $3\sigma$  detection, with a broad line of a width of 15.7  $\text{km s}^{-1}$  that had a line profile similar to those of millimeter CO lines. The line width of [C II] implies that ionic lines can come from a low-velocity C-shock.

5. We have mapped a large-scale molecular cloud structure surrounding the SNR G357.7+0.3 using the  $^{13}\text{CO}(1-0)$  line that typically traces cold clouds. The supernova component at  $-31 \text{ km s}^{-1}$  (integrated over  $-21$  to  $-41 \text{ km s}^{-1}$ ) appears to be bounded by molecular gas that is located at its southern, western, and north-western portions. We show broad molecular and carbon line detections in its northwestern portions, and possible extended interaction sites may be found toward western and southern portions with future observations.

6. We compare shock models with the observed  $\text{H}_2$  emission. A two C-shock model yielded the best fit over a one component shock model or a combination of C-shock and J-shock models. The best fit model of two slow C-shock models; a C-shock model with a density of  $10^4 \text{ cm}^{-3}$  and a velocity of  $10 \text{ km s}^{-1}$ , and a second component of C-shock with a density of  $10^5 \text{ cm}^{-3}$  and the same velocity of  $10 \text{ km s}^{-1}$ . G357.7+0.3 also lacks ionic lines in the IRS spectra. Most importantly, the detection of [C II] using SOFIA GREAT shows the FWHM is  $\sim 16 \text{ km s}^{-1}$  comparable to those of millimeter CO lines. All these facts show evidence of C-shocks and against the presence of J-shocks.

7. We estimate the CO density, column density, and

temperature by running RADEX models, using an average velocity width of 17.3 km/s. The best fit yields  $n(\text{H}_2) = 1.7^{+0.8}_{-0.5} \times 10^4 \text{ cm}^{-3}$ ,  $N(\text{CO}) = 5.6^{+0.1}_{-0.1} \times 10^{16} \text{ cm}^{-2}$ ,  $T = 75^{+30}_{-15} \text{ K}$ . This model is consistent with the upper limit of CO(11-10) brightness.

G357.7+0.3 shows broad CO lines for  $4.5' \times 5'$  area and the broad lines may extend to NE and to SW, beyond the area covered by our observations. The interaction area showing CO broad lines and  $\text{H}_2$  emission is large so the pattern of the molecular cloud interaction with the SNR may be similar to those of the well-known molecular SNRs of IC 443 and W44. It would be worthwhile to extend the millimeter maps such as CO and infrared maps in  $\text{H}_2$  which would reveal the entire regions of interaction between the SNR and molecular clouds. The newly discovered molecular cloud interaction with SNR G357.7+0.3 offers many exciting opportunities of astrophysical laboratory to study dynamics of shocks, molecular astro-chemistry, and high-energy phenomena in shocks and dense environment.

We thank Sebastien Bardeau, a staff scientist at IRAM for helping with various issues of CLASS softwares, and Miguel Angel Requena Torres and Friedrich Wyrowski for helping with SOFIA and APEX observations and data processing, respectively. We thank anonymous referee for helpful comments. The Arizona Radio Observatory is part of the Steward Observatory at the University of Arizona and receives partial support from the National Science Foundation. Based [in part] on observations made with the NASA/DLR Stratospheric Observatory for Infrared Astronomy. SOFIA Science Mission Operations are conducted jointly by the Universities Space Research Association, Inc., under NASA contract NAS2-97001, and the Deutsches SOFIA Institut under DLR contract 50 OK 0901. APEX is a collaboration between the Max-Planck-Institut für Radioastronomie, the European Southern Observatory, and the Onsala Space Observatory.

## REFERENCES

- Abdo, A. A., Ackermann, M., Ajello, M., Baldini, L., Ballet, J., Barbiellini, G., Baring, M. G., Bastieri, D. et al. 2009, *ApJ*, 706, L1
- Abdo, A. A. et al. 2010a, *ApJ*, 712, 459 (IC 443)
- Abdo, A. A. et al. 2010b, *Science*, 327, 1103 (W44)
- Abdo, A. A. et al. 2010c, *ApJ*, 718, 348 (W28)
- Aharonian, F. et al., 2008, *A&A*, 490, 685
- Anderl, S., Gusdorf, A., & Güsten, R., 2014, *A&A*, 569, 81
- Andersen, M., Rho, J., Reach, W. T., Hewitt, J. W., & Bernard, J. P., 2011, *ApJ*, 742, 7
- Arikawa, Y., Tatematsu, K., Sekimoto, Y., & Takahashi, T. 1999, *PASJ*, 51, L7
- Barber, R. J., Tennyson, J., Harris, G. J., & Tolchenov, R. N., 2006, *MNRAS*, 368, 1087
- Burton, M. G., Hollenbach, D. J., Haas, M. R., Erickson, E. F., 1990, *ApJ*, 355, 197
- Burton, M. G. & Hollenbach, D. J., 1992, *ApJ*, 399, 563
- Chevalier, R. A., 1999, 511, 798
- Daniel, C. & Slane, P., 2010, *ApJ*, 717, 372
- Draine, B. T., Roberge, W. G. & Dalgarno, A., 1983, *ApJ*, 264, 485
- Draine, B. T., 2003, *ARA&A*, 41, 241
- Dubner, G., Giacani, E., Reynoso, E., Parón, S., 2004, *A&A*, 426, 201
- Esposito, J.A., Hunters, S.D., Kanbach, G., & Sreekumar, P., 1996, *ApJ*, 461, 820
- Faure, A. & Josselin, E., 2008, *A&A*, 492, 257
- Flower, D. R. & Pineau Des Forêts, G., 2010, *MNRAS*, 406, 1745
- Frail, D. A. et al. 1996, *AJ*, 111, 1651
- Gray, A.D., 1994, *MNRAS*, 270, 835
- Hanabata, Y., Katagiri, H., Hewitt, J. W. et al., 2014, *ApJ*, 786, 145
- Heyminck, S., Grad, U.U., Güsten, et al, 2012, *A&A*, 542, L1
- Hewitt, J. W., Rho, J., Andersen, M., & Reach, W. T., 2009, *ApJ*, 694, 1266
- Hewitt, J. W., Yusef-Zadeh, F., Wardle, M., 2008, *ApJ*, 683, 189
- Hewitt, J. W. et al. 2012, 759, 89
- Hewitt, J. W. & Lemoine-Goumard, M. 2015, *High-energy gamma-ray astronomy*, eds. B. Degrange, G. Fontaine, vol.1
- Hollenbach, D. & McKee, C. F., *ApJ*, 1989, 342, 306 (HM89)
- Hollenbach, D. Kaufman, M.J, Bergin, E. A., & Melnick, G.J., 2009, *ApJ*, 690, 1497
- Huang, Y.-L. & Thaddeus, P., 1986, *ApJ*, 309, 804
- Jeong, I.-G. et al., 2013, *ApJ*, 770, 105
- Kaufman, M.J., & Neufeld, D. A. 1996, *ApJ*, 456, 611
- Kawasaki, J. et al., 2005, *ApJ*, 631, 935
- Kilpatrick, C.D., Biegging, J.H., & Rieke, G.H. 2014, *ApJ*, 796, 144
- Kilpatrick, C.D., Biegging, J.H., & Rieke, G.H. 2016, *ApJ*, 816, 1 (scheduled) or arXiv:1511.03318
- Kristensen et al. 2010, *A&* 521, L30
- Kristensen et al. 2012, *A&* 542, 8
- Koo, B.-C., & Moon, D.-S., 1997, *ApJ*, 485, 263
- Koo, B.-C., Rho, J., Reach, W. T., Jung, J., & Mangum, J. G., 2001, *ApJ*, 552, 175
- Ladd, N., Purchell, C., Wong, T., & Robertson, S., 2005, *PASA*, 2005, 22, 62
- Lazendic, J. S., Slane, P. O., Hughes, J. P., Chen, Y., Dame, T. M., 2005, 618, 734
- Lazendic, J. S., Wardle, M., Whiteoak, J.B., Burton, M. G., & Green, A.J., 2010, *MNRAS*, 409, 371
- Leahy, D. A., 1989, *A&A*, 216, 193
- Lesaffre, P., Chiéze, J.-P., Cabrit, S., & Pineau des Forêts, G., 2004a, *A&A*, 427, 147
- Lesaffre, P., Chiéze, J.-P., Cabrit, S., & Pineau des Forêts, G., 2004b, *A&A*, 427, 157
- Liszt, H. S. & Lucas, R., 1998, 337, 246
- Liszt, H. S. & Lucas, R., 1998, 339, 561
- Liszt, H. S., 2009, *A&A*, 508, 1331L
- Neufeld, D. A. et al., 2006, *ApJ*, 649, 816
- Neufeld, D. A. et al., 2007, *ApJ*, 664, 890
- Neufeld, D. A., Gusdorf, A., Güsten, Rolf, Herczeg, G. J., Kristensen, L., Melnick, Gary, J., Nisini, B., Ossenkopf, V., Tafalla, M., van Dishoeck, E. 781, 102
- Orlando, S. Bocchino, F., Miceli, M., Reale, F., & Peres, Mem. S.A.It. suppl. 13, 97
- Pannuti, T.G., Rho, J., Heinke, C. O. & Moffitt, W. P., 2014, *AJ*, 147, 55
- Phillips, J. P., Ramos-Larios, G., & Perez-Grana, J.A., 2009, *MNRAS*, 397, 1215
- Phillips, J. P. & Marquez-Lugo, R.A., 2010, *MNRAS*, 409, 701
- Reach, W.T., and Rho, J., 1998, *ApJ*, 507, 93L
- Reach, W.T., and Rho, J., 1999, *ApJ*, 511, 836
- Reach, W. T., & Rho, J.-H. 2000, *ApJ*, 544, 843
- Reach, W. T., Rho, J., Tappe, A. et al., 2006, *AJ*, 131, 1479,
- Reich, W. & Fürst, E., 1984, *A&AS*, 57, 165
- Rho, J., Hewitt, J. W., Boogert, A., Kaufman, M. & Gusdorf, A., 2015, *ApJ*, 812, 44
- Rho, J., Jarrett, T., Reach, W. T., & Cutri, R., 2001, *ApJ*, 547, 885
- Rho, J. & Petre, R., 1998, *ApJ*, 503, L167
- Rho, J., Petre, R., Schlegel, E. M., and Hester, J.J., 1994, *ApJ*, 430, 757
- Reach, W. T., Rho, J., 1999, 511, 836
- Reach, W. T., Rho, J., Jarrett, T. H., 2005, *ApJ*, 618, 297
- Richter, M.J, Graham, J.R., & Wright, G. S., 1995, *ApJ*, 454, 277
- Roelfsema, P.R. et al., 2012, *A&A*, 537, 17
- Seta, M., Hasegawa, T., Sakamoto, S., Oka, T., Sawada, T., Insutsuka, S., Koyama, H., & Hayashi, M. 2004, *AJ*, 127, 1098

- Sezer, A., Gök, F., Hudaverdi, M. & Ercan, E. N. 2011a, MNRAS, 417, 1387
- Shelton, R. L., Kuntz, K. D., & Petre, R. 2004, ApJ, 615, 275
- Shinn, J.-H. et al., 2010, AdSpR, 45, 445
- Slane, P., Chen, Y., Lazendic, J. S., Hughes, J. 2002, ApJ, 580, 904
- Smith, J.D.T., Draine B.T., et al., 2007, ApJ, 656, 770
- Snell, R.L., Hollenbach, D., Howe, J.E., Neufeld, D. A., Kaufman, J.J., Melnick, G.J., 2005, ApJ, 620, 758
- Sezer, A., Gök, F., Hudaverdi, M. & Ercan, E. N. 2011a, MNRAS, 417, 1387
- Tennyson, J., Zobov, N.F., Williamson, R., Polyansky, O. L., & Bemath, P. F., 2001, J. Phys. Chem. Ref. Data, 30, 735
- Tilley, D.A., & Balsara, D.S., 2006a, ApJL, 645, 49
- Tilley, D.A., Balsara, D.S. & Howk, J.C. 2006b, MNRAS, 371, 1106
- Uchiyama, Y., Blandford, R. D., Funk, S., Tajima, H. & Tanaka, T. 2010, ApJ, 723, L122
- van Dishoeck, E. F., Jansen, D.J., & Phillips, T.G., 1993, A&A, 279, 541
- van Dishoeck, E. F. et al., PASP, 123, 138
- van der Tak, F.F.S., Black, J. H. Schöier, F.L, Jansen, D.J., van Dishoeck, E. F., A&A, 468, 627
- Wootten, H. A., 1977, ApJ, 216, 440
- Wu, J. H. K. et al., 2011, ApJL, 740, L12
- Yamauchi, S., Koyama, K., Kinugasa, K., Torii, K., Nishiuchi, M., Kosuga, T., Kamata, Y., 1998, Astron. Nachr, 319, 111
- Young, E.T., Becklin, E.E., Marcum, P. M. et al. 2012, ApJ, 749, L17
- Yusef-Zadeh, F., Goss, W.M., Roberts, D. A., Robinson, B., & Frail, D. A., ApJ, 527, 172
- Zhou, X. et al., 2011, ApJ, 791, 109
- Zhou, X. et al., 2014, ApJ, 743, 4